Investigation of Baffled Shock Tubes for Low Velocity Ram Accelerator Start

Desiree Bernhard

A thesis
submitted in partial fulfillment of the
requirements for the degree of

Master of Science in Aeronautics & Astronautics

University of Washington

2023

Committee:

Carl Knowlen, Chair

Robert Breidenthal

Program Authorized to Offer Degree:
Aeronautics & Astronautics

University of Washington

Abstract

Investigation of Baffled Shock Tubes for Low Velocity Ram Accelerator Start

Desiree Bernhard

Chair of the Supervisory Committee:
Carl Knowlen
Department of Aeronautics & Astronautics

The ram accelerator is a hypervelocity launcher in which a projectile is injected into stationary tubes filled with premixed fuel and oxidizer. Combustion is initiated as the projectile passes, creating a high pressure base that travels with it to produce thrust. To start the ram accelerator process, the projectile must be injected into the mixture at a minimum Mach number. Preliminary investigations from previous work indicate successful ram acceleration can be achieved by accelerating the propellant towards the projectile, ultimately reducing the projectile's entrance velocity while keeping the same in-tube Mach number. Accelerating propellant towards an oncoming projectile for a baffled tube ram accelerator configuration was investigated. Experimental shock wave propagation data were collected from a baffled shock tube and a computational fluid dynamics simulation was constructed in ANSYS Fluent. Experimental data provided estimates for pressure ratios, diaphragm burst times, and diaphragm scoring configurations for a low velocity start configuration. Both experimental and numerical results showed strong shock wave attenuation throughout the baffles, with a 75% strength reduction in 13 diameters compared to a smooth bore case. The contact surface velocities from the simulation provided a wave arrival time in the driven section used to time with a projectile bursting the entrance diaphragm. The results of this investigation designed an experiment to establish initial proof of concept for low velocity start in methane-oxygen with carbon dioxide and methane-air-oxygen mixtures.

TABLE OF CONTENTS

LIST OF FIGURES

LIST OF TABLES

NOMENCLATURE

A: Area, m^2

A_{throat}: Area based on projectile throat diameter, m^2

A_{tube}: Area based on bore diameter, m^2

a: Speed of sound, m/s

c_v: Specific heat at constant volume, J/kg/K

E: Total energy per unit mass, J/kg

F: Body force per unit mass, N/kg

h: Height, m

I: Inertia, kg·m^2

M: Molar mass, kg

M_S: Shock Mach number

M_{2S}: Mach number of shock-processed gas

M_{sdu}: Sonic diffuser unstart Mach number

m: Mass, kg

n: Number of moles

P: Pressure, Pa

$\dot{q}$: Rate of heat released per unit mass, W/kg

R: Universal gas constant, 8.314 J/mol/K

R_Z: Coefficient of reflection

T: Temperature, K

T_Z: Coefficient of transmission

t: Time, s

u: Velocity, m/s

v: Specific volume, m^3/kg

Z: Specific acoustic impedance, $kg/m^2/s$

α: Angular acceleration rad/s^2

γ: Specific heat ratio

θ: Angular position, rad

λ: Thermal conductivity, W/m/K

ρ: Density, kg/m^3

σ: Standard deviation

τ: Shear stress, Pa

τ_F: Torque, N·m

$\bar{x}$: Sample mean

ACKNOWLEDGMENTS

I first and foremost would like to thank my advisor, Professor Carl Knowlen, not only for sharing infinite gas dynamic knowledge, life wisdom, and ram accelerator stories but for giving me an opportunity to be a part of the Ram Accelerator Lab itself. I feel incredibly fortunate to have had mentorship from such an expert in this field who's life work constantly inspires me. I am beyond grateful for the knowledge and help you've given me over the past couple years.

As a member of my reading committee and as my former compressible flow professor, I would like to thank Professor Robert Breidenthal for providing insight and taking interest in this work. Your compressible flow lectures and stories started my grad career off strong and will not be forgotten.

To my fellow graduate students - John Correy, Jason Ginos, Richard Egbert, Cullen Yancey, Brian Leege - I equally attribute my knowledge learned from the ram lab to getting to work alongside all of you. Each one of you are brilliant engineers on your own, and I couldn't have asked for a better group of students to conduct ram shots, hammer out baffles, and listen to Halo stories with. I thank you all for not only sharing your engineering insights, but your niche interests. Even more so, I specifically would like to thank you for demonstrating great fortitude in cleaning out the catcher tube. The ram lab was never a dull time.

Operations in the lab would not be possible without all the help from all undergrads (of which there are too many to name) - you all deserve a massive thank you for your contributions. Each one of you has elevated the lab with your own engineering strengths and helped make the environment so enjoyable.

I would also like to thank my all my friends and family who've supported me on this journey and encouraged me in times of doubt. I wouldn't have been able to achieve any of

this if it were not for your support, and I hope take pride in my work. You are all invaluable to me.

Finally, I would like to thank the sponsor HyperSciences for funding this research, and in particular my deepest thanks to Mark Russell. Your support and encouragement has been fundamental to my engineering career and helped me develop my own passion in compressible flow.

DEDICATION

to my family Debbie, Scott, and Scotty...

Chapter 1

INTRODUCTION

The ram accelerator is a novel hypervelocity launcher developed by researchers at the University of Washington in the 1980s [1, 2]. The accelerator utilizes a similar aerothermodynamic propulsive cycle as that of a conventional airbreathing ramjet engine to launch projectiles up to ultrahigh velocities. To date, experimental configurations have demonstrated ram projectile masses being launched to muzzle velocities of up to 2.7 km/s, while theoretical estimations allow over 1000 kilograms be accelerated up to 9 km/s [3, 1]. The ram accelerator offers significant benefits over traditional guns by creating a more uniform thrust profile, as the projectile constantly rides the region of highest pressure throughout the tube. The system at its core is a simple chemical propulsion engine with no moving parts, making it a unique solution for alternative space launch [2, 3, 1].

1.1 Thermally-Choked Ram Accelerator

Several velocity regimes of ram accelerator operation exist: i.e., subdetonative, transdetonative, and superdetonative. This paper will focus on ram accelerator operation within the subdetonative velocity regime, in which the thermally choked propulsive model has most extensively been studied and the projectile travels at velocities lower than the Chapman-Jouguet (CJ) detonation wave speed of the propellant mixture [4]. Information on the other propulsive modes are discussed by Knowlen et al. [5] and Higgins [4].

The thermally choked ram accelerator (TCRA) propulsive cycle is analogous to that of a supersonic airbreathing, subsonic combustion ramjet engine [6] (Figure 1.1[7]). In summary, ramjets are initially accelerated up to supersonic speeds by an alternate propulsive source. The ramjet intake then diffuses the supersonic air over the centerbody, forming a system of oblique shocks and rendering the flow subsonic behind the inlet and into the combustion chamber. Fuel is then injected into the combustion chamber, and combustion is initiated

and stabilized with flame holders before being expanded through a nozzle to produce thrust.

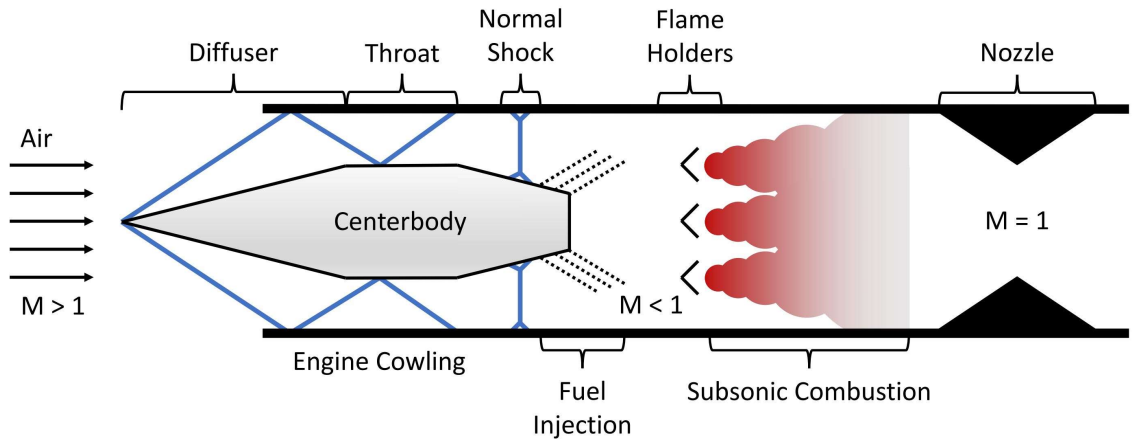

Figure 1.1: Ramjet engine cycle.

In the case of ram accelerators, the ram projectile is analogous to the center body of a ramjet while the tube walls are the outer cowling, as shown in Figure 1.2[7].

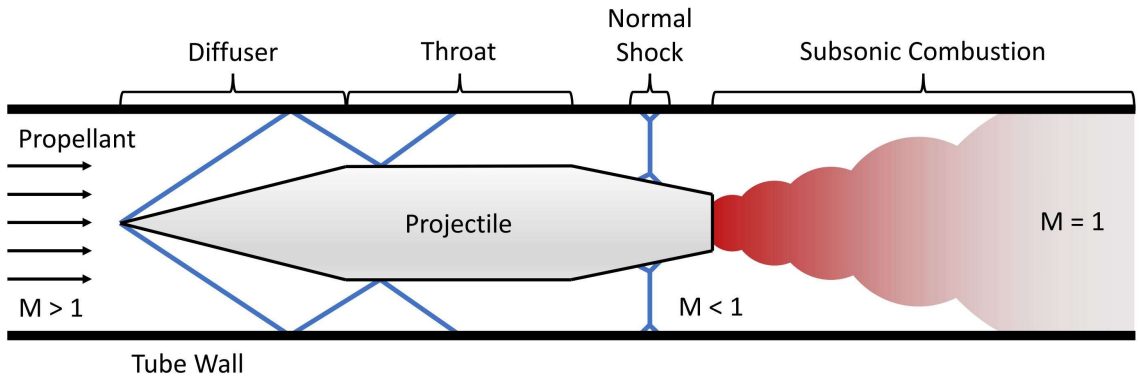

Figure 1.2: Thermally choked ram accelerator cycle.

The TCRA propulsive cycle begins when a start gun launches the projectile up to speed and injects it into the ram stages at a specified Mach number. To maintain operation in the Mach number range of 3 to 4 as the projectile accelerates, the ram accelerator launcher is partitioned into stages having gaseous propellants with increasing speed of sound that

are separated by diaphragms. Thus, the projectile holds no onboard propellant. The start gun velocity is chosen such that the Mach number is greater than one at the throat (point of minimum flow area and maximum projectile diameter) of the projectile, accounting for non-isentropic shock effects on the supersonic compression in order to start the diffuser. The nosecone angle is determined such that the system of oblique shocks from the diffuser are weak enough to not initiate combustion at the Chapman-Jouguet detonation speed of the propellant (typically 10-15 degrees), giving a typical starting Mach number in the range of 2.3-2.8 depending on the propellant mixture and projectile geometry [6]. The shock train between the projectile body and tube wall continues along the length of the projectile. Eventually, the shock train is terminated as the gas is further processed by an oblique shock on the aftbody of the projectile, ultimately rendering the flow subsonic [4].

An obturator is most commonly placed behind the projectile as it is launched from the start gun (Figure 1.3). The obturator utilizes a Bridgman seal; i.e, gun pressure expands the flared base of the obturator to effect a tight bore seal, to prevent blow-by of start gun gasses around the sub-caliber projectile from pressurizing and pre-bursting the entrance diaphragm. The obturator also acts as a piston upon entering the ram stage, first getting the stagnant ram stage gasses up to speed with the projectile and second acting as a blocking passage to pressurize and heat the gasses to facilitate combustion [8].

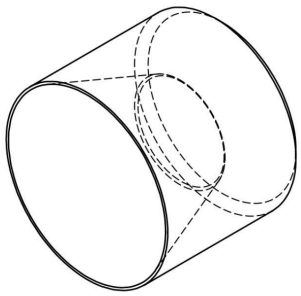

Figure 1.3: Example of an obturator used in the TRCA.

Subsonic combustion is eventually initiated by the high temperature residual launch tube gas, which is heated by multiple reflected shock waves during the launch process, that

ignites the propellant as it is being pushed forward by the obturator [9, 10, 8, 11]. The ignition process separates the projectile from the obturator and the combustion from the propellant reaches a thermally choked condition, stabilizing the normal shock train on the aftbody of the projectile. The projectile continues to accelerate forward with the highest pressure directly behind it.

1.2 Ram Accelerator Configurations

Several configurations of ram accelerator tubes exist, including the smooth-bore ram accelerator (SBRA), railed tube ram accelerator (RTRA), and baffled tube ram accelerator (BTRA). Frontal views of examples for each configuration can be seen in Figure 1.4. Smooth-bore tubes were the basis for initial ram accelerator development, in which fins were used to center and stabilize projectiles [6, 1]. The RTRA eventually offered a solution for axisymmetric projectiles, offering simplicity in projectile manufacturing without fins [12, 13, 14]. However, as ram accelerator operation theory showed that higher heat release resulted in higher thrust, the BTRA was developed in 2005 to support operation of more energetic propellants [15]. The baffled sections contain a series of washer-like inserts, effectively acting as a one-way valve that ingests the oncoming flow while preventing combustion waves from overtaking the projectile and reducing thrust [16]. An image of a projectile passing through an instrumentation insert as it was traveling through a BTRA is shown in Figure 1.5.

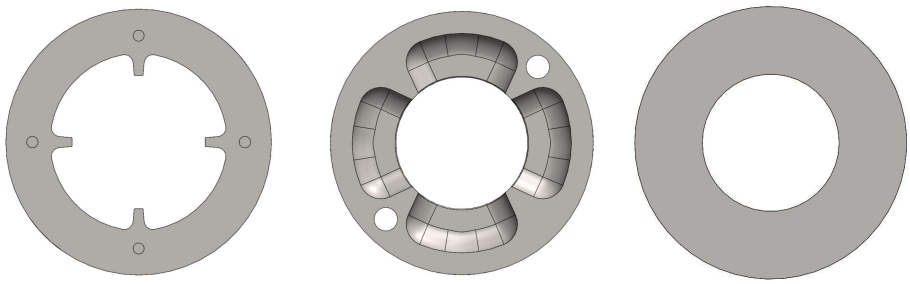

(a) RTRA (b) BTRA Insert (c) SBRA

Figure 1.4: Three frontal views of ram accelerator configurations.

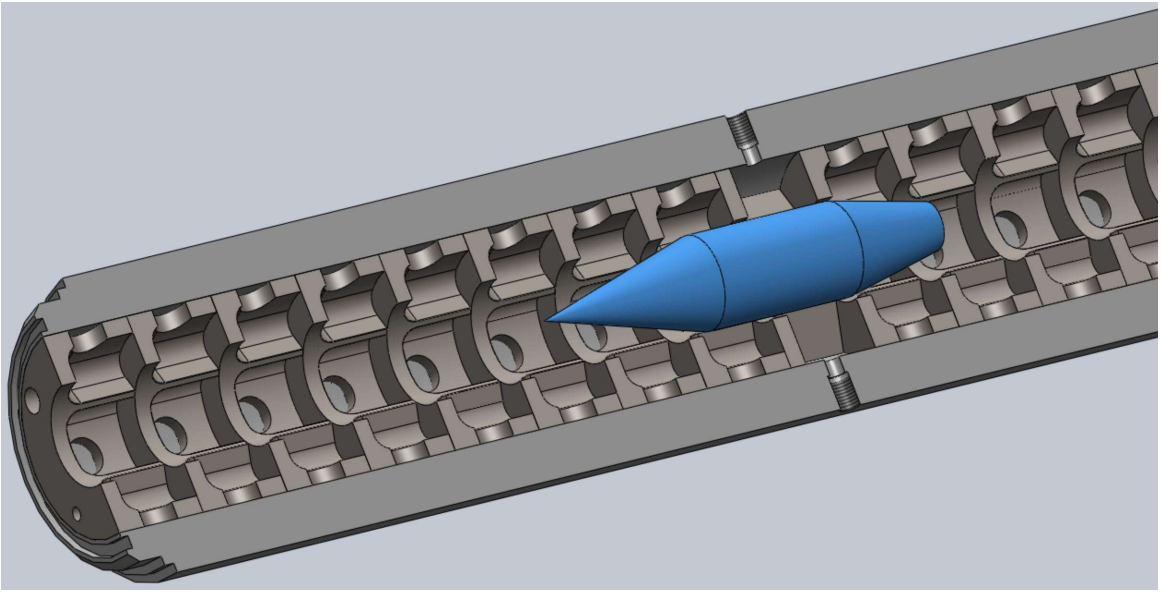

Figure 1.5: Section view of a projectile traveling through a baffled-tube.

1.3 Zero/Low Velocity Start

The starting process for ram acceleration requires some form of start gun to get the projectile up minimum operation before being injected into the ram stages. The start gun utilized by the University of Washington is a helium light gas gun, which capitalizes on the simplicity of solely using a compressed gas with high sound speed for rapid expansion. However, the helium gun comes with the high price tag of helium and is not considered an economic solution for ram accelerator use in industrial applications. An alternative option is using a combustion light gas gun with simple, industrial gases. However, the high enthalpy flow from combustion poses its own engineering challenges for rapid-fire use. A straightforward, economic solution is thus to use a compressed air gun for initial projectile acceleration [17]. Unfortunately, due to the low sound speed of air, the maximum theoretical projectile velocity via compressed air is limited to below the typical Mach numbers required for starting the ram accelerator. Thus, establishing ram accelerator operation with a reduced start gun entrance velocity is of interest, and this dilemma has a potential solution seeded in zero/low velocity start.

The concept of zero velocity start was explored by McFall et al. in the 1990s [18, 19]. Instead of launching a projectile up to velocity by means of a start gun before entering the ram stages like in traditional ram acceleration, in the zero velocity start (ZVS) concept, the projectile is initially at rest. The premixed propellants in the ram stages are separated from a tube segment containing the projectile and a low pressure gas by a diaphragm. Upon bursting the diaphragm, the propellant is expanded towards the projectile at a supersonic Mach number governed by the pressure ratio across the diaphragm. Combustion is initiated on the back of the projectile in a manner similar to that typically used for starting the TCRA propulsive mode, then the projectile accelerates forward through the expanding gasses until eventually overtaking the lead expansion wave and entering a quiescent propellant mixture [18]. Zero velocity start has so far only been theoretically investigated.

The concept of low velocity start (LVS) is similar to that of ZVS, with the difference being that the projectile will still require some initial starting velocity by means of a start gun. However, the start gun velocities could theoretically be achieved by compressed air, as the relative velocity from the expanding gases keep the same overall Mach number when starting. The concept of expanding gasses towards an oncoming ram accelerator projectile is analogous to attaching a shock tube to the entrance of the ram stages. This paper focuses on the low velocity start technique specifically for the baffled tube ram accelerator due to its pre-existing benefits for lower Mach number starting.

Chapter 2

THEORY

The low velocity starting technique investigated in this thesis requires what is effectively a baffled shock tube attached to the entrance of a traditional ram accelerator. This chapter discusses the theory of smooth-bore shock tubes and its applications to that of a baffled shock tube. Furthermore, existing literature on shock waves propagating through baffles is explored.

2.1 Smooth-bore Shock Tube

In principle, basic shock tube operation is centered around a tube separated into a driver and a driven section (Figure 2.1).

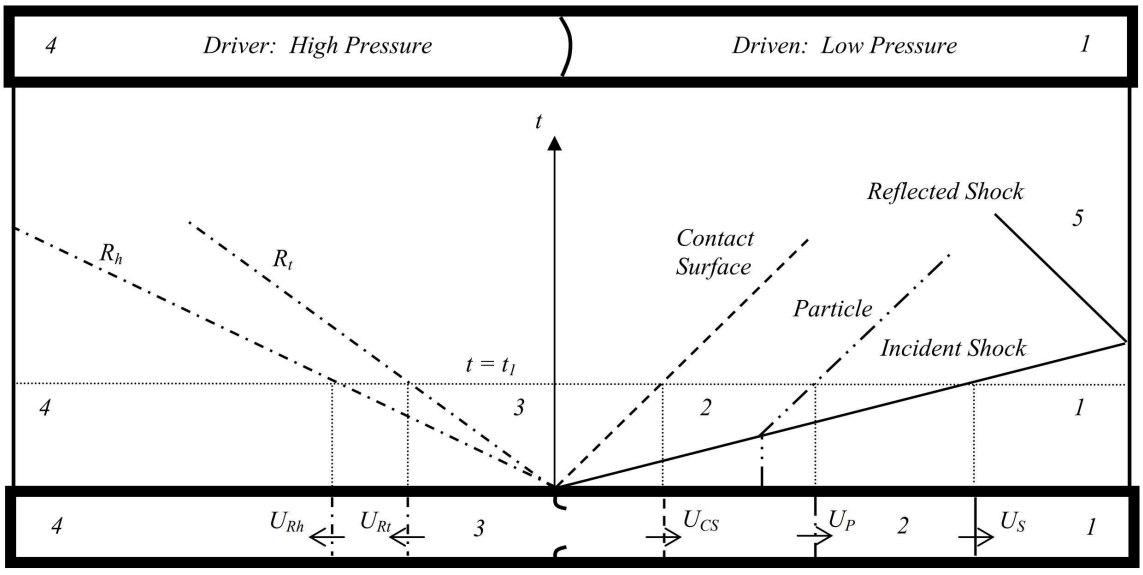

Figure 2.1: Typical smooth-bore shock tube x-t diagram.

The sections are initially separated by a thin diaphragm, and the driver and driven sec-

tions are filled with gasses to varying pressures (with the driver section being high pressure, and the driven section low pressure). Diaphragms can be made of Mylar, aluminum, or any other material that holds a specified pressure differential and bursts once that pressure differential is surpassed. Once the diaphragm bursts, the driver section expands into the driven section, generating an incident shock wave through the tube. Five regions of simple flow (i.e., constant properties) are thus developed: the untouched gas in the driver section (4), the expanded driver gas region (3), the driven gas region (2), the unprocessed gas in the driven section (1), and the reflected shock processed gas after the incident wave reaches the end of the driven section (5).

All flow of viscous fluid substances can be described by the 3D Navier-Stokes equations. The conservation of mass, momentum, and energy are defined in conservative form by eq. 2.1, 2.2, 2.3 respectively:

$$\frac{\partial \rho}{\partial t} + \overrightarrow{\nabla} \cdot (\rho \overrightarrow{u}) = 0 \tag{2.1}$$

$$\frac{\partial (\rho \overrightarrow{u})}{\partial t} + \overrightarrow{\nabla} \cdot (\rho \overrightarrow{u}\, \overrightarrow{u}) = -\overrightarrow{\nabla} \overrightarrow{p} + \overrightarrow{\nabla} \cdot \overline{\overline{\tau}} + \rho \overrightarrow{F} \tag{2.2}$$

$$\frac{\partial (\rho E)}{\partial t} + \overrightarrow{\nabla} \cdot (\rho \overrightarrow{u} E) = \rho \dot{q} + \overrightarrow{\nabla} \cdot (\lambda \overrightarrow{\nabla} T) + \rho \overrightarrow{F} \cdot \overrightarrow{u} - \overrightarrow{\nabla} \cdot (\rho \overrightarrow{u}) + \overrightarrow{\nabla} \cdot (\overline{\overline{\tau}} \cdot \overrightarrow{u}) \tag{2.3}$$

The classic smooth-bore shock tube problem assumes 1-dimensional, inviscid flow with no thermal conductivity. Thus, the equations simplify to:

$$\frac{\partial \rho}{\partial t} + \frac{\partial (\rho u)}{\partial x} = 0 \tag{2.4}$$

$$\frac{\partial (\rho u)}{\partial t} + \frac{\partial (\rho u^2)}{\partial x} = -\frac{\partial p}{\partial x} + \rho F_x \tag{2.5}$$

$$\frac{\partial (\rho E)}{\partial t} + \frac{\partial (\rho E u)}{\partial x} = \rho \dot{q} + \rho F_x u - \frac{\partial (\rho u)}{\partial x} \tag{2.6}$$

Where eq. 2.7, 2.5, 2.6 are conservation of mass, momentum, and energy respectively.

Shock tube problems involve calculating unknown flown parameters at the intermediary stages (regions 2, 3, and 5) from the initial conditions given in regions one and four. The flow variables in each region can be calculated under the ideal gas equation of state as:

$$Pv = \frac{nRT}{M} \tag{2.7}$$

The pressure, density, and temperature can then be related assuming constant entropy as shown by the isentropic gas relation in eq. 2.8:

$$\frac{P}{P_0} = \left(\frac{\rho}{\rho_0}\right)^{\gamma} = \left(\frac{T}{T_0}\right)^{\frac{\gamma}{\gamma-1}} \tag{2.8}$$

Normal shock relationships are used to determine changes of state between regions one and two. The normal shock relations to determine Mach number, density, pressure, and temperature are as follows:

$$M_{2s}^2 = \frac{2+(\gamma-1)M_s^2}{2\gamma M_s^2 - \gamma + 1} \tag{2.9}$$

$$\frac{\rho_2}{\rho_1} = \rho_{21} = \frac{(\gamma+1)M_s^2}{2+(\gamma-1)M_s^2} \tag{2.10}$$

$$\frac{P_2}{P_1} = P_{21} = 1 + \frac{2\gamma}{\gamma+1}(M_s^2 - 1) \tag{2.11}$$

$$\frac{T_2}{T_1} = \frac{a_2^2}{a_1^2} = \frac{P_{21}}{\rho_{21}} \tag{2.12}$$

The pressure ratio in eq. 2.11 is a common metric used to represent the strength of the shock. At the contact surface between the shock processed gas and expanding driver gas, the following relationships exist to determine flow variables in region 3:

$$P_3 = P_2 \tag{2.13}$$

$$u_3 = u_2 \tag{2.14}$$

$$\rho_3 = \rho_4 \left(\frac{P_3}{P_1}\right) \tag{2.15}$$

The lead expansion wave in the driver section propagates at the speed of sound of the driver gas in region 4.

Ultimately, the normal shock pressure ratio between regions 1 and 2 can be related to the diaphragm pressure ratio in regions 1 and 4 as [20, 21]:

$$\frac{P_1}{P_4} = P_{14} = \frac{1}{P_{21}}\left[1 - (P_{21}-1)\left(\frac{\beta_4 E_{14}}{\alpha_1 P_{21}+1}\right)^{\frac{1}{2}}\right]^{\frac{1}{\beta_4}} \tag{2.16}$$

Where $\beta_i = \frac{\gamma_i - 1}{2\gamma_i}$, $\alpha_i = \frac{\gamma_i+1}{\gamma_i-1}$, and $E_{14} = \frac{(c_v T)_1}{(c_v T)_4}$

The diaphragm pressure ratio can also be determined as a function of the shock Mach number by substituting eq. 2.11 in as:

$$\frac{P_4}{P_1} = P_{41} = \frac{1}{\alpha_1}\left(\frac{M_s^2}{\beta_1} - 1\right)\left[1 - \frac{\gamma_4 - 1}{\gamma_1 + 1}\frac{a_1}{a_4}\left(M_s - \frac{1}{M_s}\right)\right]^{\frac{-1}{\beta_4}} \tag{2.17}$$

2.2 Baffled Shock Attenuation Literature Review

The 1-D Euler equations presented in the smooth-bore shock tube analytical solutions no longer apply when analyzing a baffled shock tube system. The 3D Navier-Stokes equations must be re-derived for a two dimensional case, as one dimensional calculations ignore any reflected shock structures and separated flow off of baffle chambers. Pre-existing literature on 2-D shock transmission will be discussed.

The transmission of an incident shock through an orifice has been explored by Takiya et al. in 2012. The shock passed through an orifice acting as an effective baffle chamber wall with a height of 2/5 diameters. The transmitting shock diffracted through the orifice, resulting in spherical expansion due to the rapid increase in cross-sectional area. The orifice effectively acted as an obstacle to attenuate the strength of the shock front, and reflected shocks were observed off the front orifice plate and expanded wall section. However, the study only observed shock passage through one orifice, whereas the baffled shock tube in this thesis will have shock propagation through hundreds of baffles.

Detonation propagation past a series of obstacles has been studied numerous times, such as with flame visualization through a series of orifice plates [22], experimentally through rough walled tubes using fiber optics [23, 24], and using numerical simulations to model deflagration-to-detonation transition (DDT) mechanisms [25]. However, detonations produce shocks sustained by rapid combustion of the mixture, whereas the shock tube in this thesis is a case of inert gas dynamics.

Inspired by airblast propagation in tunnels, inert shock propagation in a tube with transverse ribs was explored by Craige and Haines in 1979 at Science Applications, Inc for the Defense Nuclear Agency[26]. The shell tube test section contained a 50 diameter section of shock tube with equally spaced transverse ribs having a height of 1/25 diameters (Figure 2.2). The study found shock wave attenuation and propagation velocity loss after traveling through the ribs and highlighted the complicated reflected shock structure off of each surpassing rib. The shallow height of the ribs created interest in their interactions with boundary layer growth, but the study concluded the ribs did not significantly affect the boundary layer growth rate.

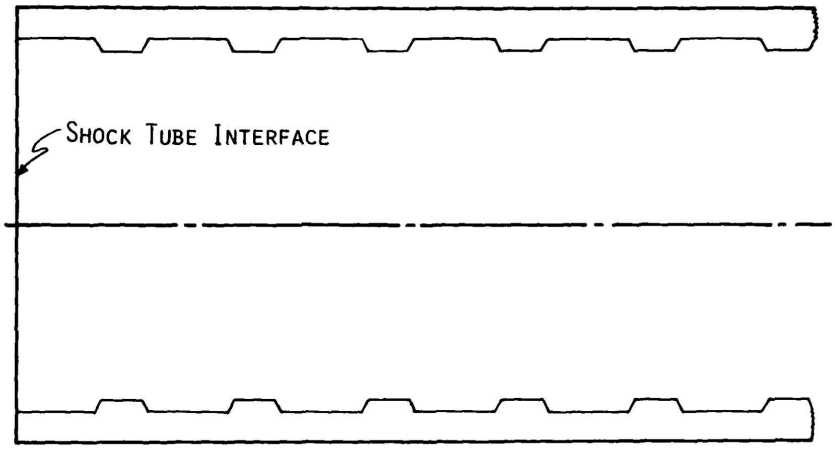

Figure 2.2: Rib geometry utilized in the airblast trench study.

Under the same ribbed shock tube analysis, shock strength attenuation was found to be dependent upon initial shock strength, with high shock strengths (pressure ratios of greater than 300) decaying to half their smooth wall values in twenty diameters and lower shock strengths decaying less rapidly [27]. Additionally, the experimental shock tube data was found to be scalable towards a much larger tube size (such as that of a tunnel). The experiments found no discern-able effect of Reynolds number from the flow on shock attenuation or on pressure waveforms when the Reynolds number was changed by an order of magnitude [27]. Two-dimensional calculations using the finite difference Air Force Weapons Laboratory HULL code [28] were able to show the complex structure from rib interactions and showed shock decay occurring more rapidly than an equivalent free air burst, but lacks any influence of viscosity.

Despite similarities of shock attenuation over several repeated geometries, the shallow height of the ribs do not translate effectively over to the large flow separation, turbulent cavity flow, and shock propagation attenuation associated with the rib (baffle wall) heights of 1/5 diameters in the BTRA. Thus, no literature has been found at the time of writing that accurately describes the flow phenomena explored in this thesis.

Chapter 3

EXPERIMENTAL FACILITY & METHODS

This chapter details the capabilities of the University of Washington ram accelerator facility.

3.1 Lab Facility

The ram accelerator facility consists of three major room spaces: the apparatus lab space, the gas bunker, and the control room bunker.

The apparatus lab space contains all mechanical hardware associated with the energetic system. It consists of a helium light gas gun, helium dump tank, ram accelerator test section, drift tube, and final catcher tank to decelerate the projectile (Figure 3.1). The helium gun is 6-m-long with a 38-mm-bore diameter, capable of accelerating 150 g up to 1.2 km/s [29]. An evacuated dump tank following the start gun provides a space for the expansion of helium gas, helping prevent premature bursting of the entrance diaphragm from blow-by and interference with the ram starting process.

Following the dump tank and vent tube is the 16-m-long ram accelerator test section supported by roller bearings on an I-beam to allow for recoil, ease of access, and maintenance. The test section for operations of interest consists of four, 2-m-long shell tubes that can be individually separated with diaphragms. Each 2 m shell holds 56 baffle inserts with a 38-mm-bore diameter and a 76-mm-outer diameter. The shell tubes can accommodate baffles, rails, or any combination when operating with an axisymmetric projectile. Instrumentation stations are placed at five equidistant positions across each shell, with each station consisting of a pair of instrumentation ports 180 degrees from one another.

Following the exit of the final shell tube, the projectile enters 8 m of smooth-bore evacuated drift tube that guides it into the final dump tank and catcher tube. The final dump tank captures remaining combustion products and its catcher tube is filled with high

energy absorbing materials for sudden projectile deceleration. The rear of the catcher tube can be opened for retrieval of any projectile remains.

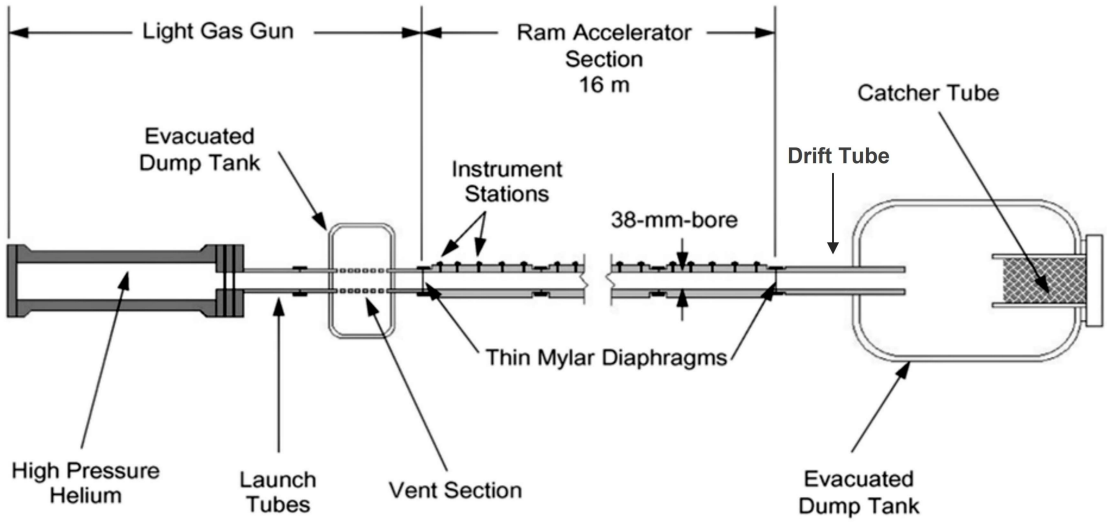

Figure 3.1: UW Ram accelerator test facility components.

The gas bunker is separated from the experimental apparatus and is where the gas bottles are stored. Gasses include oxidizers, inerts, and fuels that flow through a mass flow control system and eventually into the ram stages. Each mass flow controller is set to operate at the desired partial pressure of each propellant component and the gasses are co-flowed through any number of the three fill lines into the desired ram stage. The 8-m-long BTRA test section can be loaded through filling ports at multiple locations, and/or the individual tubes can be partitioned into stages of various lengths and loaded independently (Figure 3.2). The mass flow controllers have a factory rated uncertainty of 2% throughout their operable range. Routine calibrations over a narrow mass flow rate range are conducted to reduce uncertainty to 1% for each component, resulting in 2% uncertainty for the propellant mole ratios [7].

A control bunker provides the operating space for all personnel during experiments. It contains the data acquisition system, the mass flow controller panel for setting gas flow

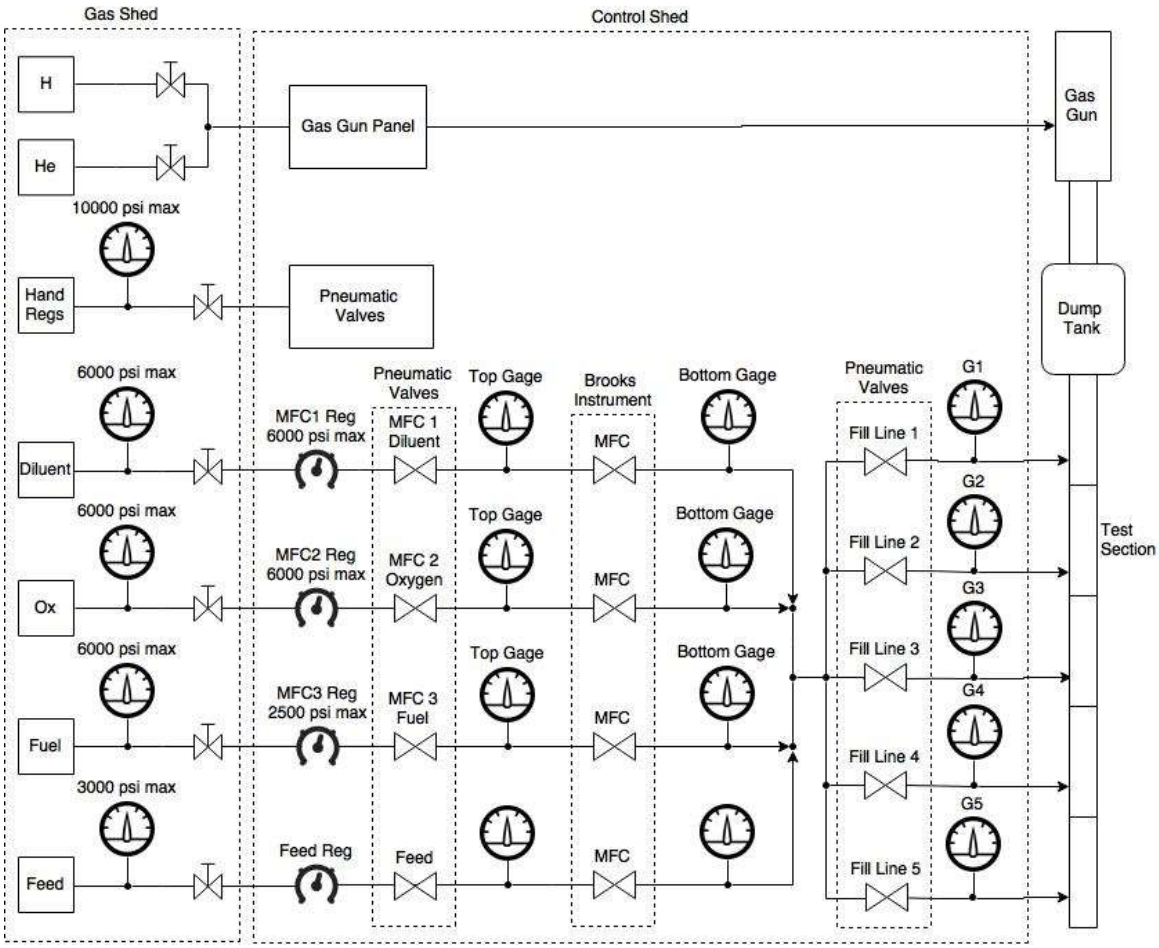

Figure 3.2: UW mixing panel P&ID.

rates, hand regulators and gauges to adjust pressures, and switches to operate fill valves to the system. All operations of the start gun are handled in the control bunker. Additionally, a vacuum system is utilized to evacuate the entire system before filling propellants into the ram stages. This includes all ram stages, the launch tube prior to the test section, the drift tube after the test section, and both the final dump tank and catcher tube. The vacuum system is also monitored and operated from within the control bunker.

3.2 Baffle Inserts

The current ram accelerator configuration uses four 2-m-long shell tubes, providing an overall test section length of 8 m. Each tube has an inner diameter of 76 mm, with the first and second tubes (BT1 and BT2) having outer an diameter of 114 mm and the third and fourth tubes (BT3 and BT4) having an outer diameter of 152 mm [30, 31]. During the test series investigated in this thesis, the shell tubes contain three different baffle inserts: the BTRA 501, the BTRA 501s, and the BTRA 111 as shown in Figure 3.3.

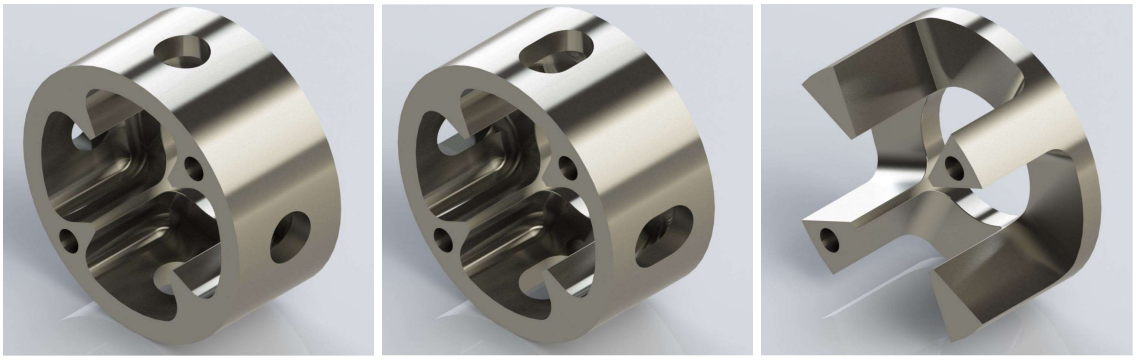

(a) BTRA 501 Insert (b) BTRA 501s Insert (c) BTRA 111 Insert

Figure 3.3: Three baffle geometries.

Each insert has a length of 35.7 mm and baffle walls normal to the direction of flow that are 6.4-mm-thick. The 501 baffle insert has a 63.5-mm-inner chamber diameter and two pairs of opposing access ports with diameters of 14.3 mm. The 501s baffle insert has the same dimensions, with the exception of a slotted instrumentation port for additional

clearance. The 111 baffle insert has an open chamber with rails extending from the baffle with an effective inner chamber diameter of 76 mm (shell tube inner diameter).

The overall baffle configuration in the test section is presented in Figure 3.4. The first shell tube has 45 BTRA 111 inserts at its entrance that provide the minimum starting and operating Mach number capability of the test section. Following the entrance baffles are ten BTRA 501 inserts and one 111 at the instrumentation station for BT1. BT2 and BT3 each have 51 BTRA 501 inserts and a BTRA 111 insert located at each of the five instrument stations. Finally, 20 BTRA 501 inserts were placed in BT4 followed by 31 BTRA 501s inserts, again with BTRA 111 inserts placed at each instrumentation station. The BTRA 111 inserts allow additional clearance for instrumentation in case of any baffle shifting during normal ram accelerator operation.

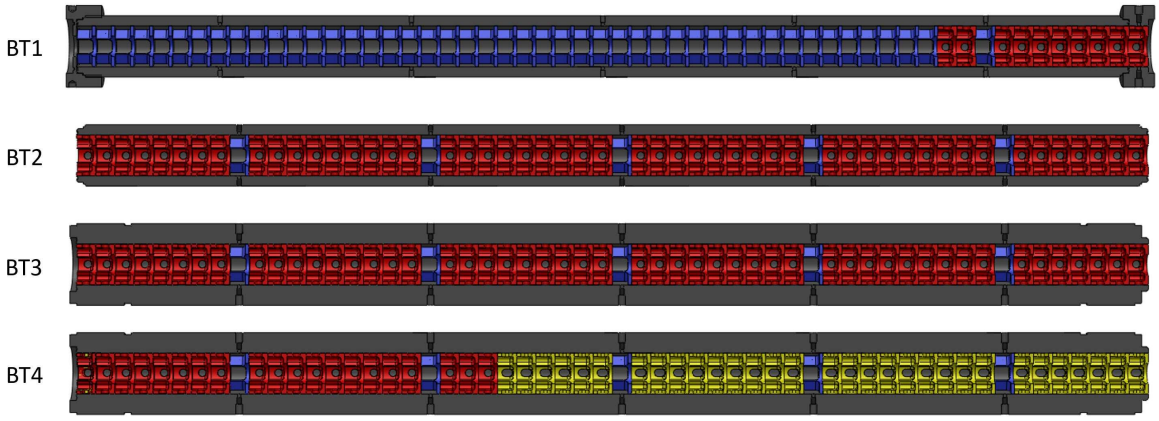

Figure 3.4: Current baffle configuration. Blue = BTRA 111, Red = BTRA 501, Yellow = BTRA 501s .

3.3 Projectiles

Projectiles used in the BTRA system are axisymmetric and typically manufactured from 6061-T6 aluminum alloy or polycarbonate. Projectiles have varying nose angles, aft angles, and shoulder lengths depending on the goals of the test series. Some example projectile configurations are displayed below in Figure 3.5. P380-1.7BL refers to a projectile diameter

of 1.380 inches (25.1 mm) and length 1.7 times the length of one baffle. Longer body projectiles have applications in alternative space launch due to a larger cargo space, while shorter projectiles may be more appropriate for repetitive impact drilling. Longer body projectiles may also contribute to greater combustion effectiveness in the baffle chambers, generating higher thrust [32].

Typical diametric clearance between the shoulder diameter of the projectile (35.1 mm) and baffle inner diameter (38.1 mm) is 3 mm. The rear of the projectile is drilled out, where a neodymium magnet is placed to detect the passage of the projectile through the test system by in-house built electromagnetic (EM) probes [33]. Projectile masses fabricated from polycarbonate range from 120 g to 260 g, whereas aluminum projectiles are approximately 265 g in the P380-1.7BL configuration [29].

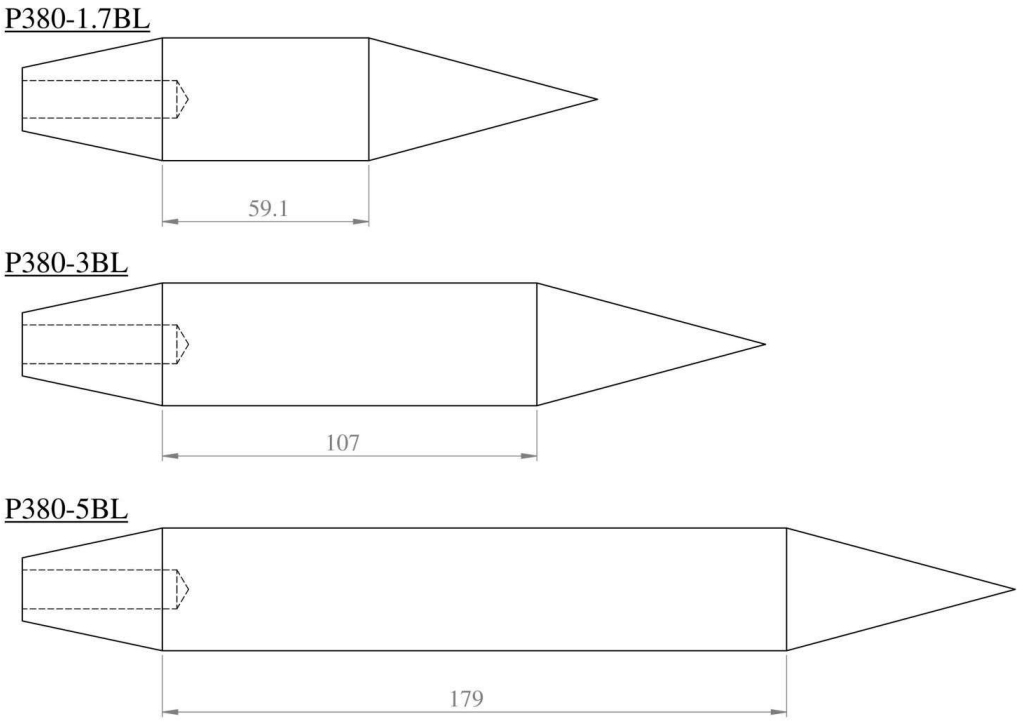

Figure 3.5: Ram projectile configurations with varying shoulder length.

3.4 Instrumentation

PCB model 119B11 piezoelectric pressure transducers were utilized to track shock wave time-of-arrival and sidewall pressure data. These transducers were recessed by 6.35 mm at varying locations throughout the tube, with instrumentation ports existing every 357.1 mm. PCB model 402M99 impedance converters were coupled with the transducers, giving the transducers an overall response time of 1 microsecond. The laboratory frame wave velocity can thus be derived from the shock wave time-of-arrival and distance between the transducers. Data were collected and recorded by a National Instruments PXIe-1071 chassis with two PXIe-6358 modules, sampling at 1.25 MHz for ram accelerator operation and 100 kHz for the test series described in Chapter 4.

Chapter 4

EXPERIMENTAL TEST CONFIGURATIONS

Experimental data on baffled shock tube wave speeds were gathered in the ram accelerator facility. Two main test series were conducted; the first focused on controlled bursting of a double-diaphragm configuration and the second focused on defining the pressure ratio of interest and coining parameters that promote fast and complete opening of diaphragms. Combustible propellants are the end goal when coupling the baffled shock tube to a ram system for low velocity start, but inert gasses were initially used to examine the wave dynamics of the system.

4.1 Controlled Diaphragm Bursting

The first test series first consisted of a 2-m-long smooth-bore driver section and a 2-m-long baffled driven section as shown in Figure 4.1. Details on the baffle configuration can be found in Section 3.2. Each end was sealed off with metal endplates, and a double-diaphragm setup was designed and implemented in-between the two stages (Figures 4.2 and 4.3).

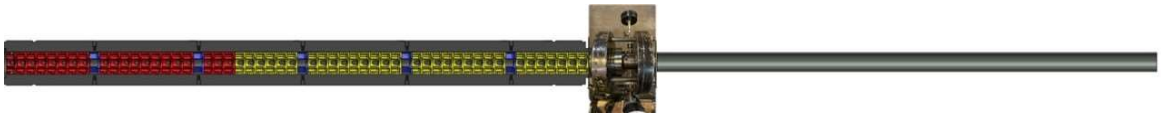

Figure 4.1: Test configuration 1: 2-m-long baffled driven (left), inner diaphragm configuration (middle), 2-m-long smooth-bore driver (right).

The inner diaphragm setup consisted of two 63.5 mm diaphragms on each side of the insert (Figure 4.4). Flanges couple the stages together and were easily accessible for quick repeated diaphragm replacement. The inner volume between the two diaphragms was filled to an intermediary pressure between the driver and driven pressures. A fill line connected the inner volume to the driver stage, separated by an air-actuated needle valve.

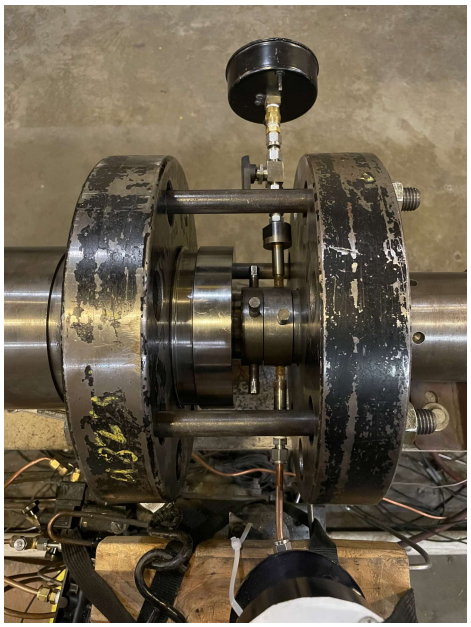

Figure 4.2: Double-diaphragm configuration between the driver (right) and driven (left) sections. The inner volume gauge and its isolation valve are also shown.

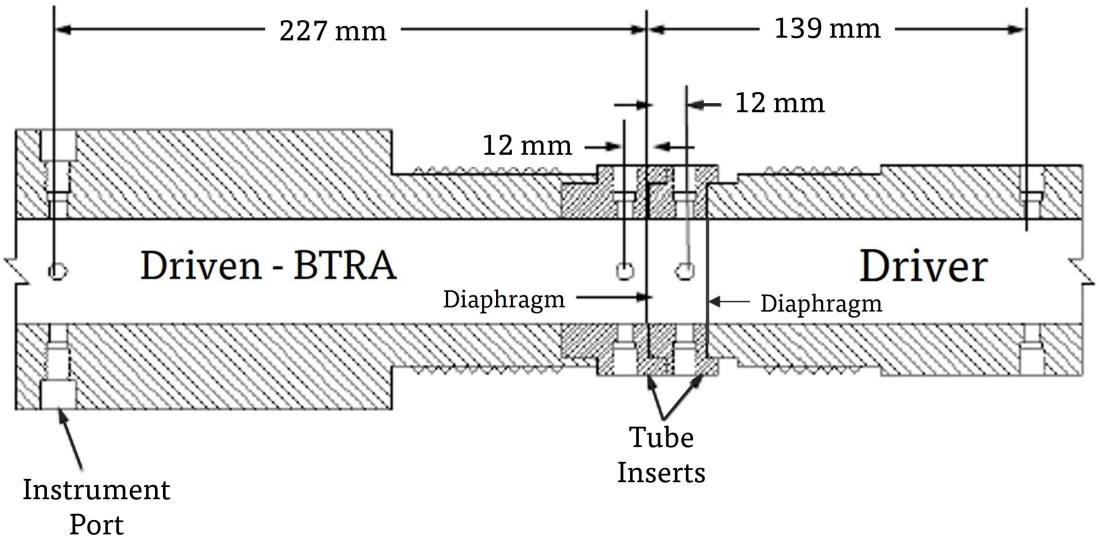

Figure 4.3: Schematic of the double-diaphragm configuration. Tube inserts not to scale.

(a) Upstream driver diaphragm, post-shot. (b) Downstream driven diaphragm, pre-shot.

Figure 4.4: Driver and driven diaphragms seen on each side of the insert.

On command, opening the needle valve pressurized the inner diaphragm. The downstream diaphragm bursts, which immediately vents the inner diaphragm volume to the point where the upstream diaphragm burst pressure is exceeded, which bursts the upstream diaphragm and ultimately starts the shock expansion into the driven section. The inner volume section had the same 38.1-mm-inner diameter as the smooth-bore tube and was 30-mm-long.

The order of operations to conduct a test was as followed:

1. Evacuate all stages.
2. Fill driven section to pressure of interest.
3. Fill inner volume and driver section simultaneously to inner volume pressure of interest (needle valve open).
4. Close needle valve (verify pressure on manual gauge installed on inner volume).

5. Continue filling driver section to pressure of interest.
6. Send signal to solenoid to open the needle valve, equalizing pressures and beginning the shock expansion into the driven section.

Pressure transducers were placed in both the driven and driver sections to track the shock wave and expansion fan arrival in each section. To send power to the solenoid of the air-actuator for the needle valve, a solid state relay activated with a 9 V battery and switch were used. The input signal from the switch was fed into the DAQ to provide initiation time stamp for the double-diaphragm burst process. The DAQ sample rate was set at 100 kHz.

Five tests were conducted with the 2 m smooth-bore driver, 2 m baffled driven system using nitrogen in both sections. The goal of the controlled diaphragm bursting test series was to establish the timing between sending a signal to the solenoid and the upstream diaphragm bursting. This timing information will then be used to drive experiment design and establish order of operations when firing a projectile into the expanding gases, as discussed in Chapter 7. Additional goals from the test series included performing initial configuration shakedown of the system, testing instrumentation, gathering information on baffled shock front velocities, and observing diaphragm openings.

4.2 Pressure Ratio Investigation

The second main test series involved moving the double-diaphragm configuration between a 4-m-long baffled driver, 4-m-long baffled driven system (Figure 4.5) - closer to the actual configuration to be used when coupled with the ram accelerator. Again, the ends for each section were sealed off with metal end plates. Four more tests were conducted at the new system configuration using nitrogen in both sections.

Due to the restricted cross-section of the inner diaphragm volume, the flow was locally choking at the insert, restricting mass flow into the driven section and ultimately reducing the shock strength. Thus, the double-diaphragm configuration was replaced with a Mylar diaphragm to separate driven and driver stages. Note, several thicknesses of diaphragms were used and/or stacked together to hold a pressure ratio of interest. Diaphragms thick-

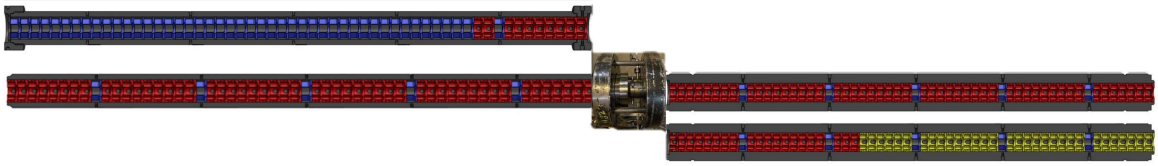

Figure 4.5: Test configuration 2: 4-m-long baffled driven (left), inner diaphragm configuration (middle), 4-m-long baffled driver (right).

nesses were a combination of 0.127 mm (0.005") and 0.381 mm (0.015"), where every 0.127 mm holds approximately 150 psi.

The order of operations to conduct a test was as followed:

1. Evacuate all stages.
2. Fill driven section to pressure of interest.
3. Fill driver section until diaphragm bursts, beginning the shock expansion into the driven section.

Pressure transducers were only placed in the driven section, as the expansion fan in the driver section was already tracked and repeatable. N2/N2 was used for 12 shots, followed by one N2/CO2 with CO2 in the driven section in order to replicate the later combustible propellants of interest.

The goal of the pressure ratio investigation test series was to establish a pressure ratio that produced a predicted particle velocity in the driven section fast enough to contribute to low velocity start. Additionally, the quality of diaphragm openings was observed and iterated on until a combination was found to produce a satisfactory opening, as partially opened diaphragms produced lower intensity shocks than fully opened diaphragms [34]. The thickness of stacked diaphragms and variations of diaphragm scoring pressures and number of scores were experimented with.

The thin 0.127 mm Mylar diaphragms opened in a multiple point configuration without any scoring. The thicker 0.381 mm Mylar diaphragms opened in a two point configuration

unless scoring lines to guide the opening were added. The most favorable scoring technique found was a cross-like configuration with a scoring pressure of 850 psig on a 0.381 mm diaphragm. Too shallow of scoring typically caused uneven openings. When stacking diaphragms, stacking multiple thin 0.127 mm diaphragms instead of using a thick 0.381 mm diaphragm was favorable. Examples of good and bad diaphragm openings are shown in Figure 4.6. Additional diaphragm results are presented in Appendix A, and the remaining experimental results from this test series are presented in Chapter 6.

(a) Partially opened diaphragm. (b) Fully opened diaphragm.

Figure 4.6: Examples of diaphragm openings.

Chapter 5

DEVELOPMENT OF CFD MODELS

A transient baffled shock tube computational fluid dynamics (CFD) model was developed to compare with experimental data and create a predictive tool for varying configurations. A classic transient Sod shock tube [35] model was first developed to calibrate the CFD parameters used in the simulation. Similar parameters were then implemented in the baffled shock tube case.

5.1 Sod Shock Tube Calibration

Transient CFD modeling of a SOD shock tube system in the laboratory frame was carried out with ANSYS Fluent computer software [36]. To begin, a 2-D axisymmetric smooth-bore shock tube was modeled with the following setup parameters:

1. 0.5 m driver, 0.5 m driven, with a 30 mm diameter.
2. Transient-explicit-density-based solver used for axisymmetric models.
3. Inviscid with energy model on.
4. Explicit Roe-FDS flux solver with explicit transient formulation: least squares cell based gradient, second order upwind flow, first order upwind turbulent kinetic energy and first order upwind specific dissipation rate.
5. Ideal gas equation of state used for air for both the driver and driven section at an initial fill temperature of 300 K and a pressure ratio of 200 (600 psia driver, 3 psia driven).
6. Walls of the tube were assigned to be adiabatic surfaces.
7. Courant number of 0.1.

The starting ANSYS configuration can be seen in Figure 5.1. Note, the shock tube simulations have the driver on the right with the driven on the left, causing the shock wave to move from right to left. This frame of reference was chosen on the basis that ram accelerator performance is typically modeled from left to right. Thus, an oncoming ram projectile (left to right) enters the expanded shock gasses (right to left) and experiences a significantly higher in-tube Mach number.

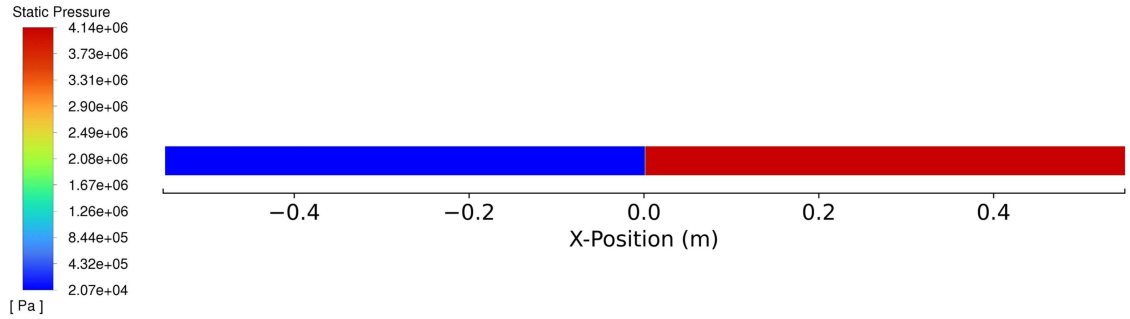

Figure 5.1: ANSYS CFD of the Sod shock tube presure distribution pre-diaphragm burst. The diaphragm is located at X=0.

The particle velocity, static pressure, static temperature, and shock front wave velocity in the laboratory frame were all tracked and compared to the analytical results. In order to track the wave velocity from the time-step static pressure outputs, a Python script was developed. The script finds the first instance that a node deviates from its initial pressure due to the incoming shock wave, uses linear interpolation to create a best fit line between that point and several others behind it, then finds the intercept of where the best fit line crosses the initial pressure. The x-location and time stamp of that file are recorded, and the script loops through all other timestamp data outputs, eventually outputting a position vs. shock velocity in the laboratory frame curve. The filtering of the data is a function of the Courant number in ANSYS, the grid spacing, the threshold at which pressure deviation is detected, the pressure file output frequency, and the number of data points chosen in the linear interpolation.

The wave velocity data from the simulation was analyzed both at 1 microsecond (the maximum fidelity of instrumentation in the lab) and filtered to 20 microseconds for comparison. The following simulation (Figure 5.2) had a cell sizing of 0.5 mm in the driven section and 1 mm in the driver. Both the filtered and unfiltered CFD data, after reaching steady state, have an average shock velocity with less than 1% error compared to the theoretical smooth-bore predictions. Thus, as the filtered data resembles the average of the unfiltered data with similar accuracy, filtered data is used as an acceptable metric representing the CFD results when presenting wave velocity.

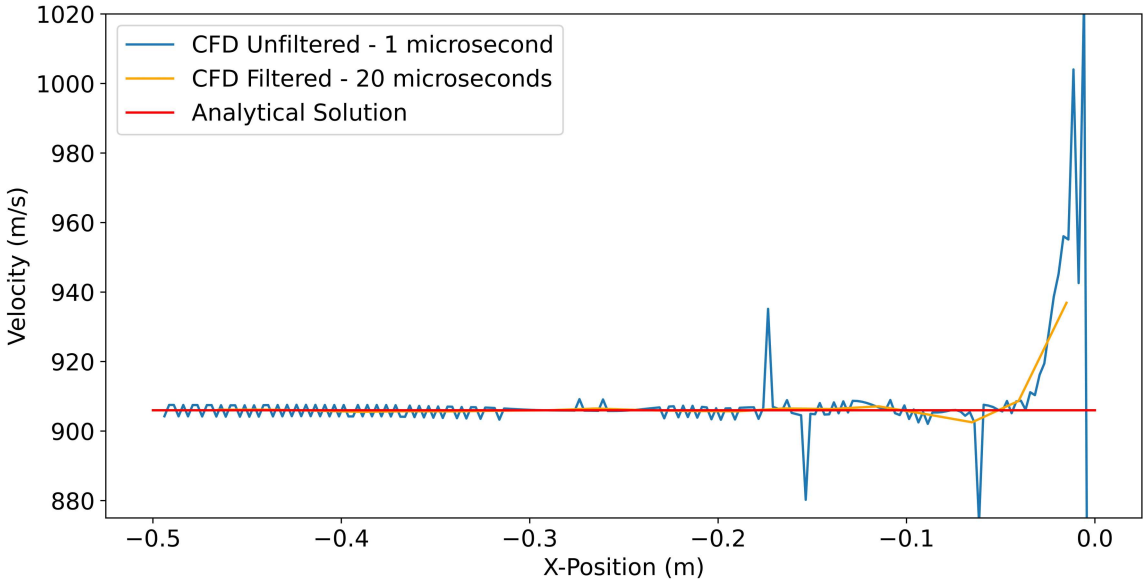

Figure 5.2: Wave velocity in the driven section for a Sod shock tube. Accuracy of filtering the output data using a wave tracking script is compared to the analytical solution.

The particle velocity, static pressure, static temperature, and density for the Sod shock tube are presented in Figures 5.3, 5.4, 5.5, 5.6 at an arbitrarily chosen flow time of 3.485 miliseconds. Regions immediately on either side of the contact surface are compared with the analytical solution.

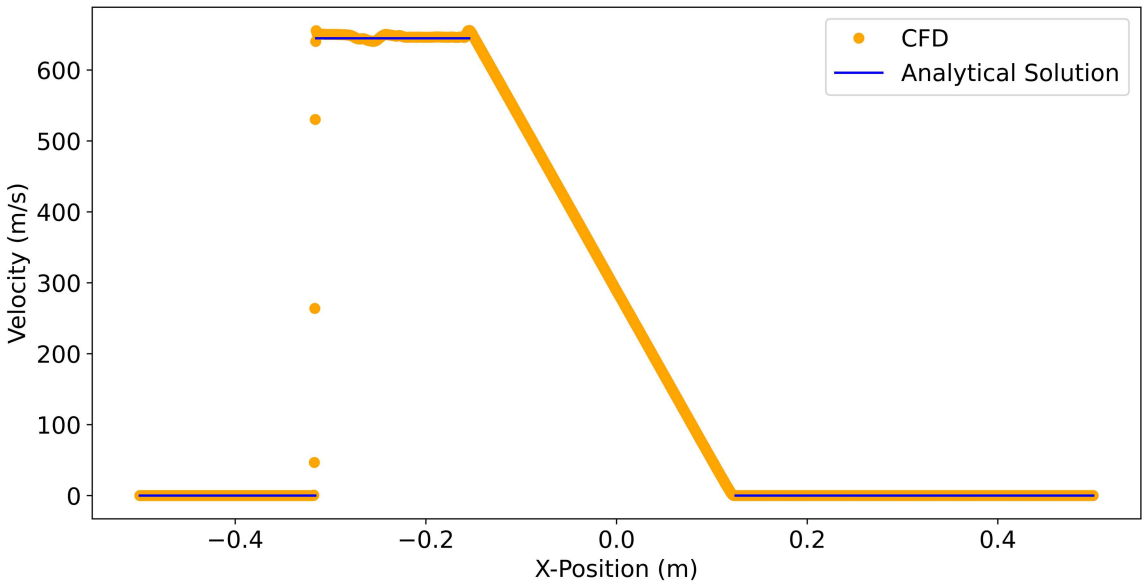

Figure 5.3: CFD vs. analytical solution for particle velocity.

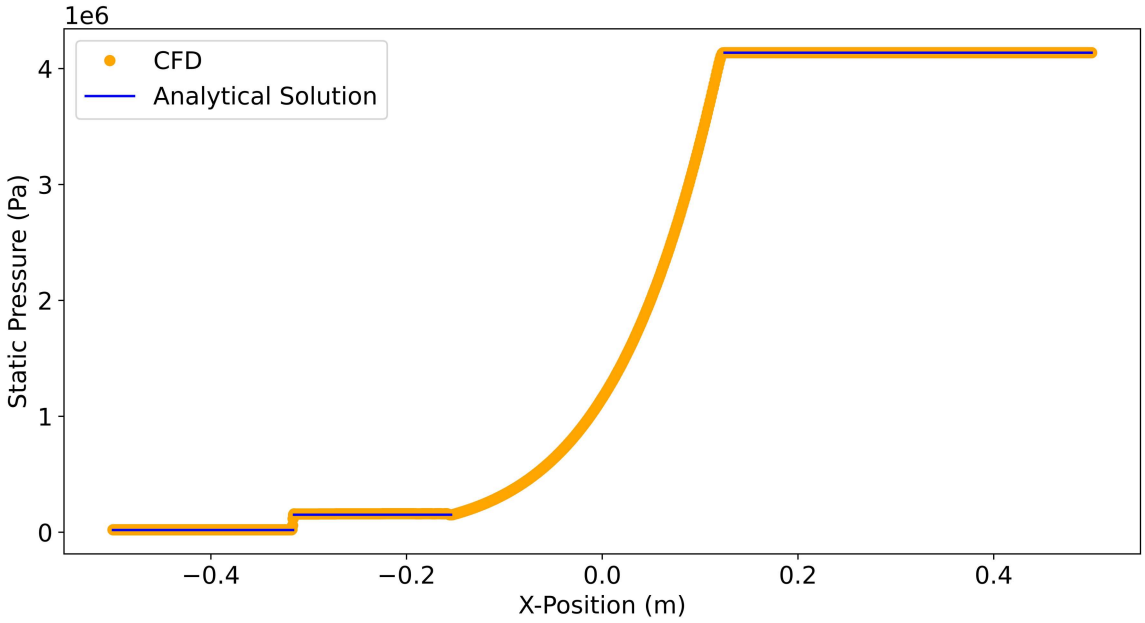

Figure 5.4: CFD vs. analytical solution for static pressure.

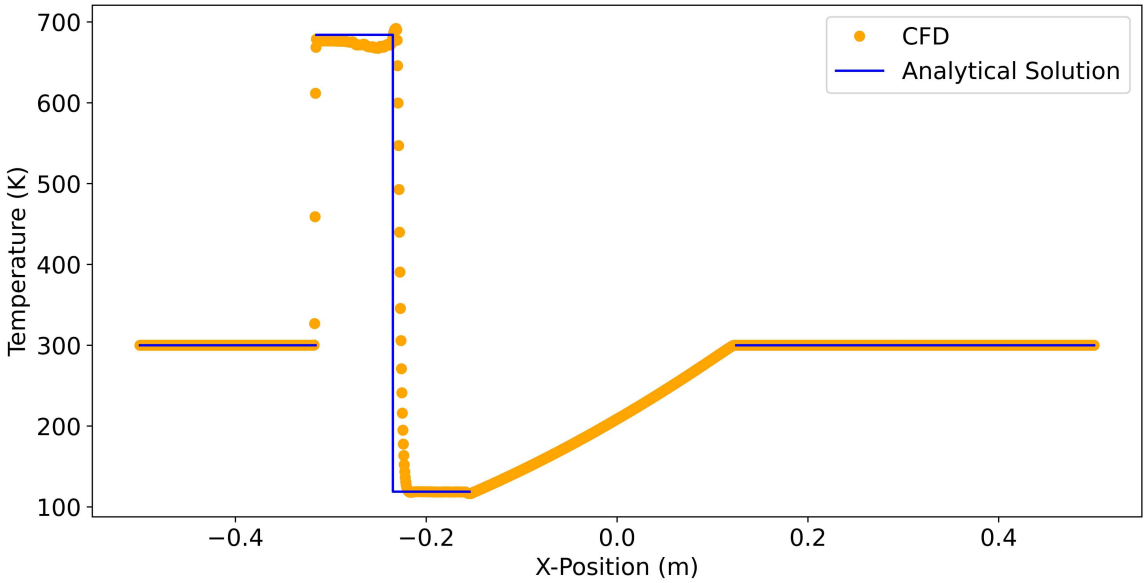

Figure 5.5: CFD vs. analytical solution for static temperature.

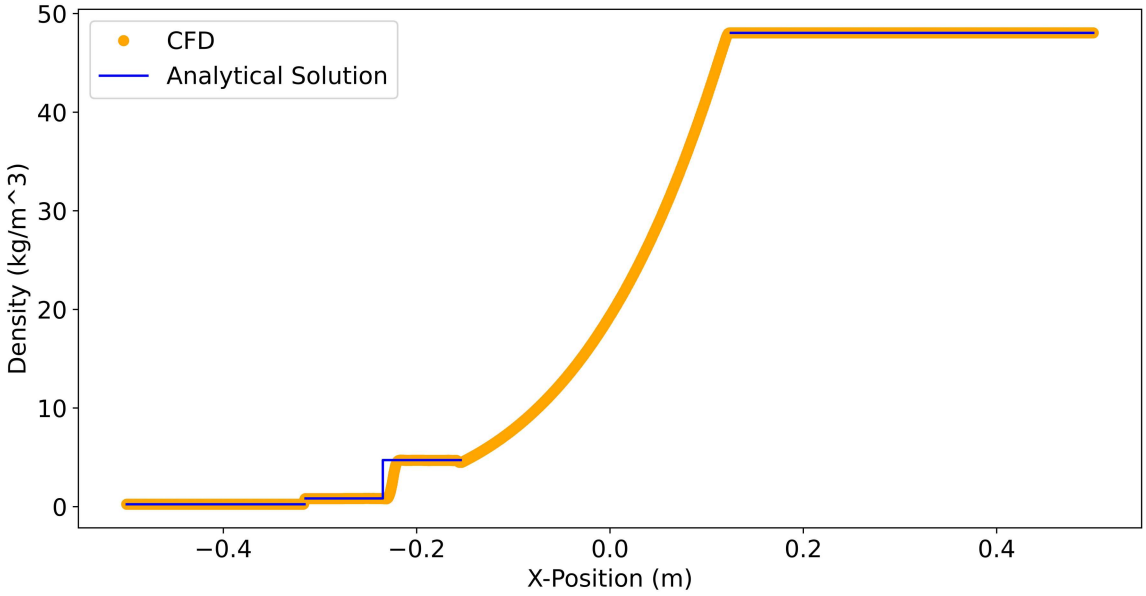

Figure 5.6: CFD vs. analytical solution for density.

The CFD results were averaged along the sections immediately on either side of the contact surface and a percent error was calculated between the region average and the analytical solution. The gradients were ignored in the averaging of the static temperature and density calculations. The results are presented in Table 5.1.

Variable	Percent Error
Particle Velocity - Regions 2 & 3	$< 1\%$
Static Pressure - Regions 2 & 3	5.01 %
Static Temperature - Region 2	1.67%
Static Temperature - Region 3	1.97%
Density - Region 2	1.36%
Density - Region 3	2.35%

Table 5.1: CFD error with analytical solution for regions 2 and 3 separated by the contact surface.

The errors compared to the analytical solutions are all less than 3%, apart from the static pressure deviation by approximately 5%. Thus, the Sod setup parameters are deemed appropriate to capture the wave dynamics in a baffled shock tube system.

5.2 General Mesh Settings

Meshing for the Sod shock tube was done in ANSYS Mechanical. The Sod shock tube configuration was meshed with the following parameters:

1. MultiZone Quad/Tri Method with all quad free face mesh type.
2. Quadrilaterals face meshing.
3. Element sizing between 0.25-4 mm in the driver and driven sections.

ANSYS requires the labeling of varying components when making and running an axisymmetric model. This involved defining the axis of rotation, walls, and inner free surfaces

(such as as "driver" and "driven") for which fluids were assigned. No inflation along the wall boundaries was used, as the flow is inviscid and lacking boundary layer development. Additionally, no dynamic meshing was used in the simulation, as stagnant meshes were shown to effective in capture the shock front as shown in the parameter calibration analysis. After creating the mesh geometry, running diagnostics after each meshing attempt including skewness, element quality, and orthogonal quality is highly recommended [37]. The mesh representing Figure 5.2 is shown below in Figure 5.7.

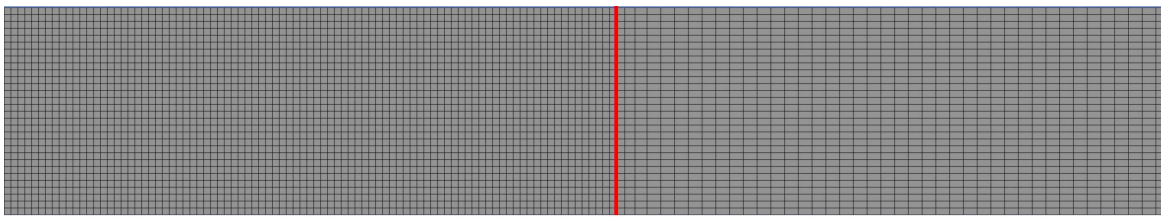

Figure 5.7: Sod mesh example with 0.5 mm elements in the driven (left) and 1 mm elements in the driver (right). The diaphragm is represented by the red line. The total mesh has 45,060 elements, 46,593 nodes, a minimum orthogonal quality of 1, a minimum element quality of 0.799, and a maximuim skewness of 4.27e-7.

A mesh independence study was conducted to determine appropriate element sizing. Element sizing ranged between 0.25 mm to 4 mm, and as the driver section only carries expansion waves with shallower gradients, reduced fidelity in the driver compared to the driven section was explored. The results for 6 mesh solutions are presented in Figure 5.8.

As the mesh sized increased, so did the transient time when initially developing the shock. However, after steady state was reached, each mesh solution had an average wave velocity in the laboratory frame of less than 1% when compared to the analytical solution. Figure 5.9 removes the larger mesh sizes for easier comparison of smaller meshes.

In application for initial testing, when coupled with an oncoming ram accelerator projectile the baffled shock tube driven section will be 6 m at the University of Washington facility. The end goal when applied for alternative space launch will potentially be hundreds of meters. Thus, the transient starting delay for the first 0.05 m in each mesh combination

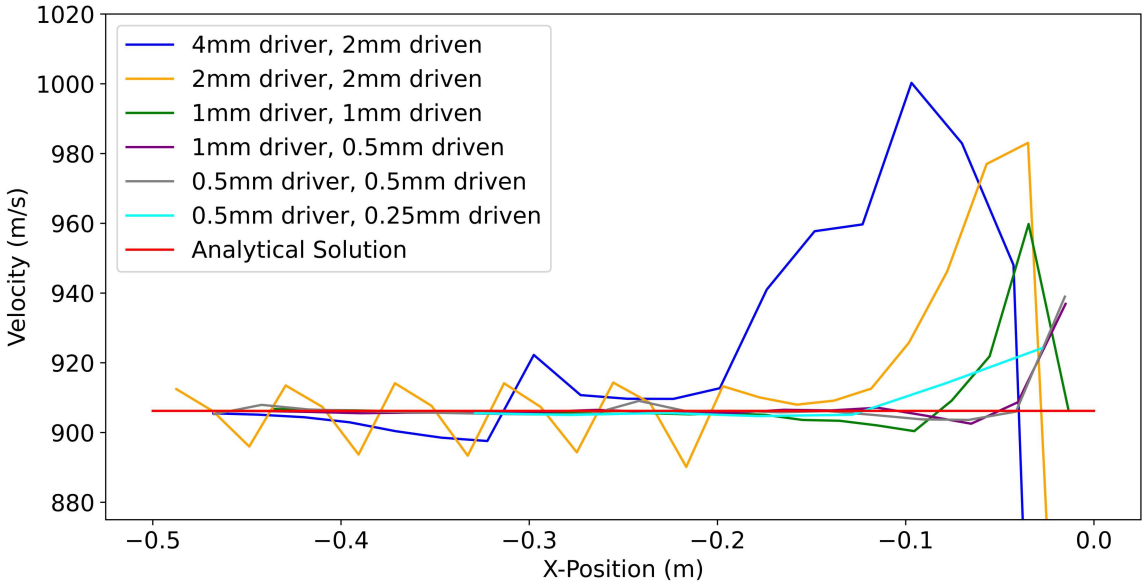

Figure 5.8: Mesh independence study on the Sod shock tube for 6 mesh sizes.

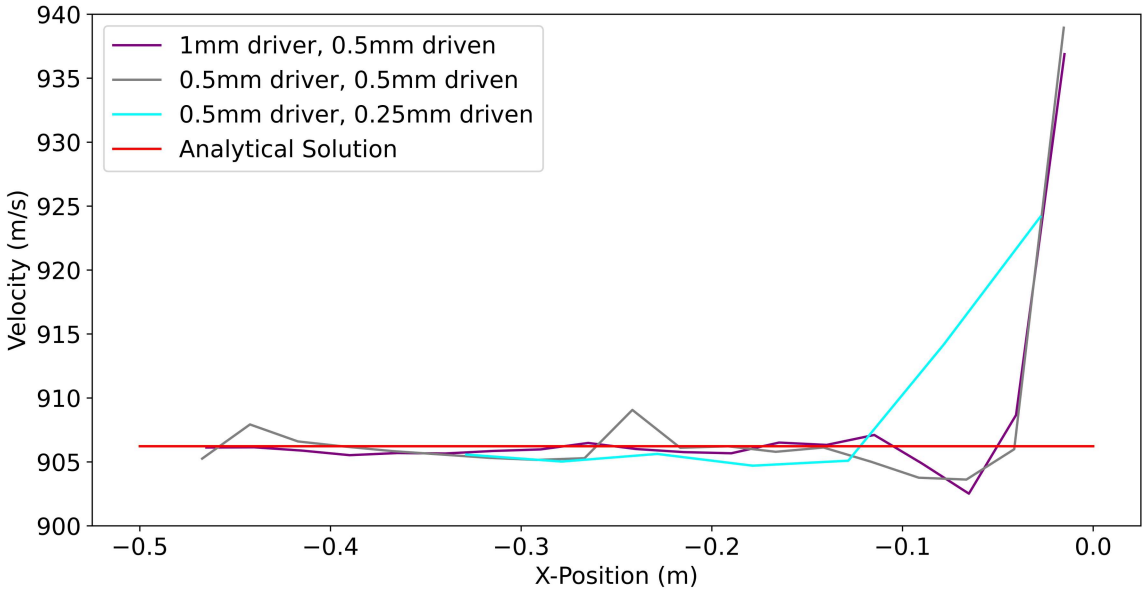

Figure 5.9: Mesh independence study comparing the three smallest mesh sizes.

in Figure 5.9 is considered to be negligible when compared to the overall goal of the CFD simulations. Any of the mesh sizes in Figure 5.9 are therefore deemed acceptable to use when simulating the baffled shock tube case.

5.3 Baffled Shock Tube Setup

Transient CFD modeling of the baffled shock tube system in the laboratory frame was developed based on the Sod calibration. An 2-D axisymmetric baffled shock tube was modeled with the following setup parameters:

1. 60 501 baffles in the driven section, 30 501 baffles in the driver.
2. Transient-explicit-density-based solver used for axisymmetric models.
3. SST $k-\omega$ turbulence model with energy and species transport models on.
4. Explicit Roe-FDS flux solver with explicit transient formulation: least squares cell based gradient, second order upwind flow, first order upwind turbulent kinetic energy and first order upwind specific dissipation rate.
5. Nitrogen and CO2 ideal-gas mixture with mixing-law specific heat, mass-weighted-mixing law thermal conductivity, mass-weighted-mixing-law viscosity, and kinetic-theory mass diffusivity.
6. Nitrogen in the driven and CO2 in the driver at an initial fill temperature of 300 K and a pressure ratio of 215.4 (582 psia driver, 2.7 psia driven).
6. Walls of the tube were assigned to be no-slip adiabatic surfaces with 0.5 standard surface roughness.
7. Courant number of 0.1.

The SST $k-\omega$ turbulence model was chosen based on it being a $k-\omega$ and $k-\epsilon$ hybrid, in which the $k-\omega$ model is used near the wall boundaries to resolve the viscous sub-layers and the $k-\epsilon$ model is used in the free-stream. Meshing for the 90 baffle configuration was chosen with 0.5 mm element sizes in the driven section and 1 mm element sizes in the driver. The total mesh has 301,100 elements, 308,457 nodes, a minimum orthogonal quality of 0.70957 (average 0.9815), a minimum element quality of 0.41228 (average 0.9647),

and a maximum skewness of 0.59075 (average 2.42e-2). Note the maximum skewness and minimum orthogonal and element qualities are located in the driver section where there is no steep shock gradient to capture. The volume of rails within the baffles were assumed to be negligible and thus removed from baffle modeling. Additionally, any rounded pockets within the baffles were approximated as sharp edges for mesh simplicity and all baffle inserts were modeled based on the 501 baffle insert geometry (Figure 4.6a). Despite viscosity being added to the baffled shock system simulation, no inflation was used along the boundaries to preserve computational efficiency. As the goals of the simulation were to track the wave and particle speeds and analyze conditions within the volume of projectile passage, any vortex dissipation within the baffle pockets near the wall boundaries was of less concern. A zoomed in view of the baffle shock tube system is shown in Figure 5.10, with a full scale model shown in Figure 5.11.

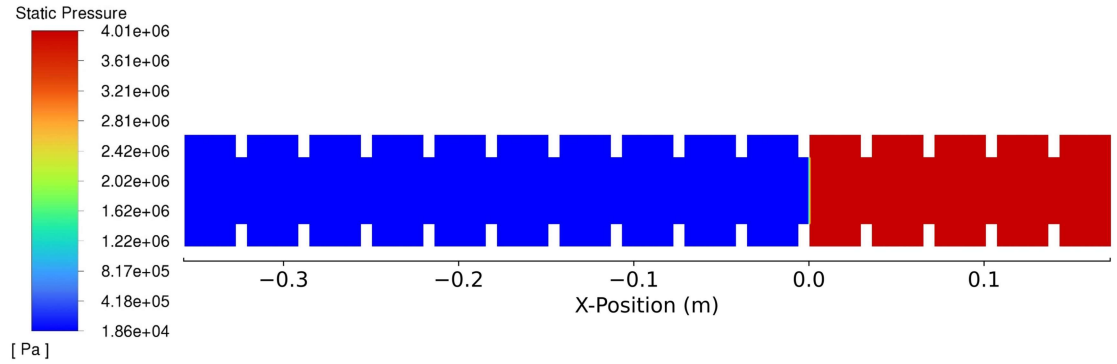

Figure 5.10: ANSYS CFD of the first 15 baffle's pressure distribution pre-diaphragm burst. The diaphragm is located at X=0.

Figure 5.11: Full graphic of the 90 baffle CFD simulation.

Chapter 6

RESULTS

The experimental wave velocity results obtained from the University of Washington ram accelerator facility are presented in this chapter in comparison with CFD results. Additionally, inert baffled tube gas dynamics are presented and analyzed from the CFD results.

6.1 Wavefront Velocity

The shock wave time-of-arrival experimental and CFD results are presented in Figure 6.1. The results correspond to a pressure ratio of 215.4, with 582 psia (4012 kPa) of nitrogen in the driver section and 2.7 psia (18.6 kPa) carbon dioxide in the driven section.

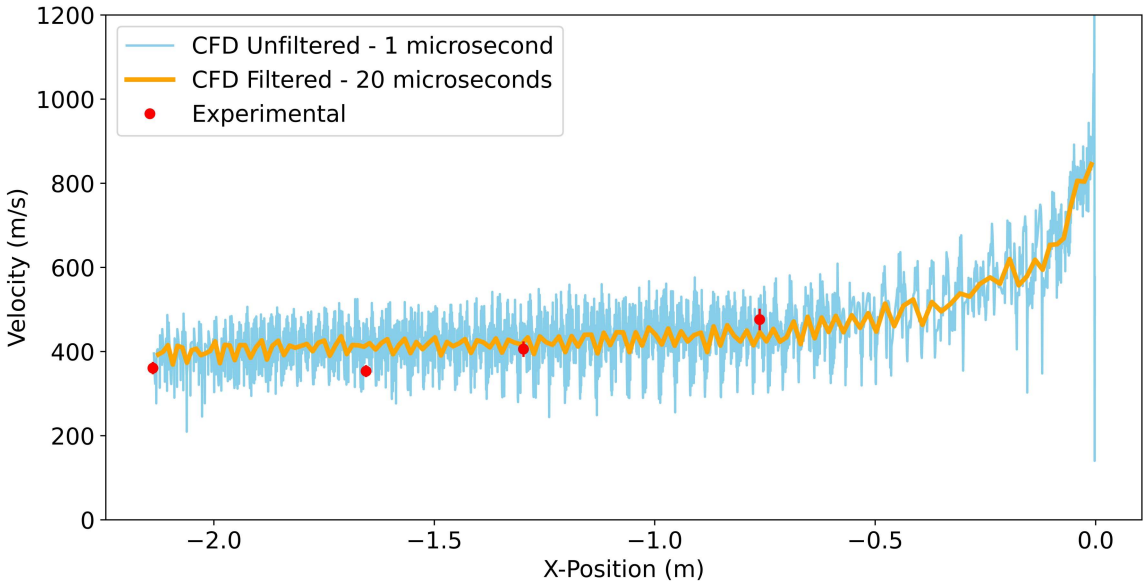

Figure 6.1: Shock wave time-of-arrival CFD vs. experimental data for a N2/CO2 driver/driven pressure ratio of 215.4.

As the shock wave passes through the baffle chambers, the resultant interaction attenu-

ates the shock as seen by exponential decrease in propagation velocity until approximately 13 chamber diameters (at an X-position of -0.8 m, passage through 22.4 baffles) based on the filtered CFD data. The wave then appears to reach a steady-state condition with only slight further decline in propagation velocity. Using linear interpolation between nodes, numerically the simulation reaches half its theoretical smooth-bore shock strength in only approximately 2.4 diameters (passage through 4.3 baffles). By the time the wave front reaches the "steady state" propagation velocity at 13 diameters, the averaged shock strength is only 1/4 of its theoretical smooth-bore strength.

The maximum uncertainty of the experimental mean velocity between two instrumentation stations is the sum of the uncertainty in separation distance between the stations, the sample rate uncertainty per probe, and the lead wave arrival time uncertainty due to signal distortion, port recess, and probe sensitivity. All uncertainties per data point are displayed using error bars on Figure 6.1, with the maximum uncertainty being 5.42%. The simulation thus captures general trends of the lead shock wave propagation velocity within an appropriate error margin to be used as an engineering tool, as all velocity data points and their respective uncertainties are within the oscillations shown in the CFD data. This gives validation of the baffled shock tube numerical method to be modified and used as a predictive tool for general trends of other pressure ratios, propellants, or baffle geometries of interest.

A zoomed in graph around the first experimental data point is shown in Figure 6.2, with the baffle wall geometry displayed underneath for reference. The unfiltered CFD data shows the shock wave propagation velocity oscillating in a stepped waveform with an amplitude of $\sim$200 m/s. As the noise in the wave tracking script for the Sod shock tube calibration was on the order of a couple meters per second ($<$1% of the propagation speed), the oscillating pattern is likely a real gas dynamic phenomenon, where the lead shock wave is constantly being accelerated and slowed down at a cycle rate equivalent to the length of one baffle.

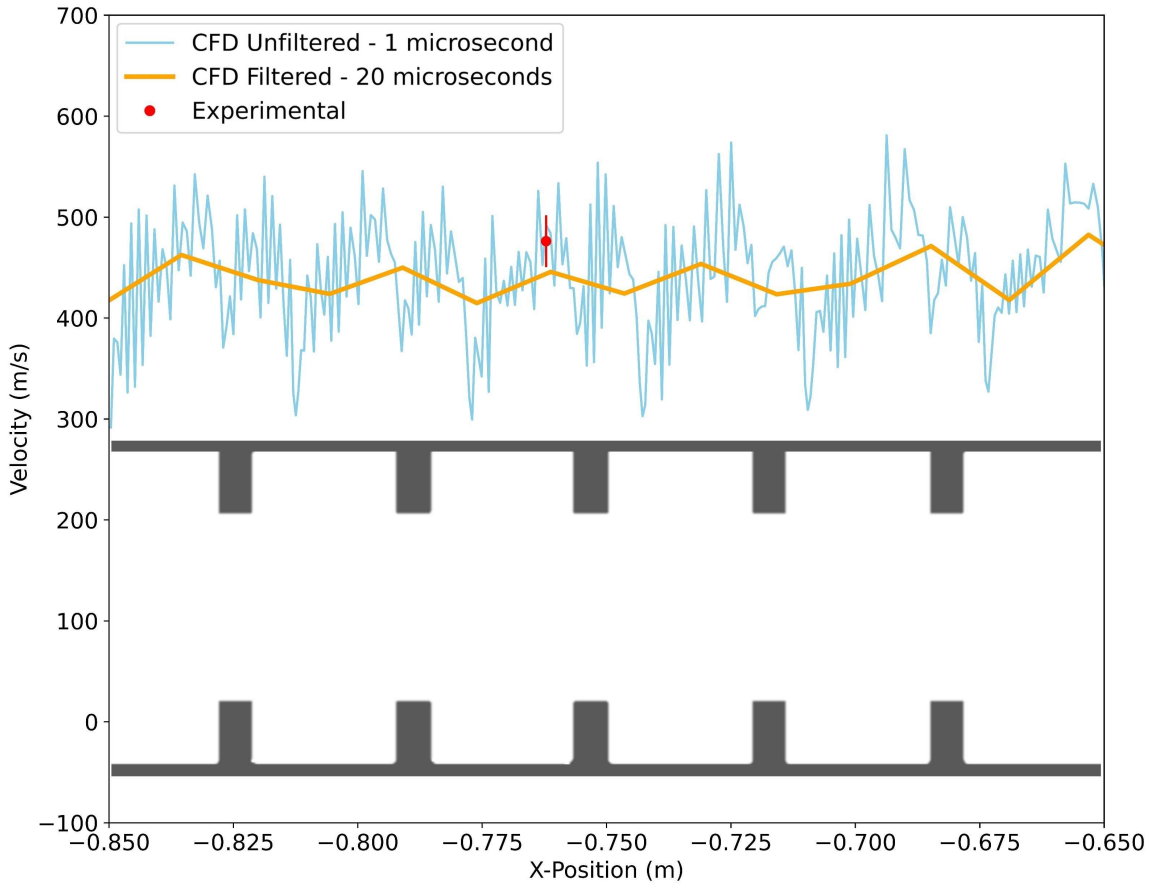

Figure 6.2: Zoomed in shock wave time-of-arrival CFD vs. experimental data. Baffle geometry is displayed underneath for reference.

6.2 Flow Field Contours

Development of the lead shock wave through the baffle inserts is presented through sequential static temperature CFD contours in Figure 6.3. The shock wave is initially developed after diaphragm breaking occurs at 0 s, where high pressure gasses from the driver expand into the driven section. Figure 6.3a shows the planar lead shock front after flowing through the first area of maximum constriction. Spherical expansion of the shock wave then develops into the baffle chamber due to rapid cross-sectional area increase as shown in Figures 6.3b and 6.3c. The spherical expansion is next hit with a second area constriction (Figure 6.3d), where the shock front diffracts through the constriction at a backwards step and an expansion wave is formed that attenuates the lead shock wave.

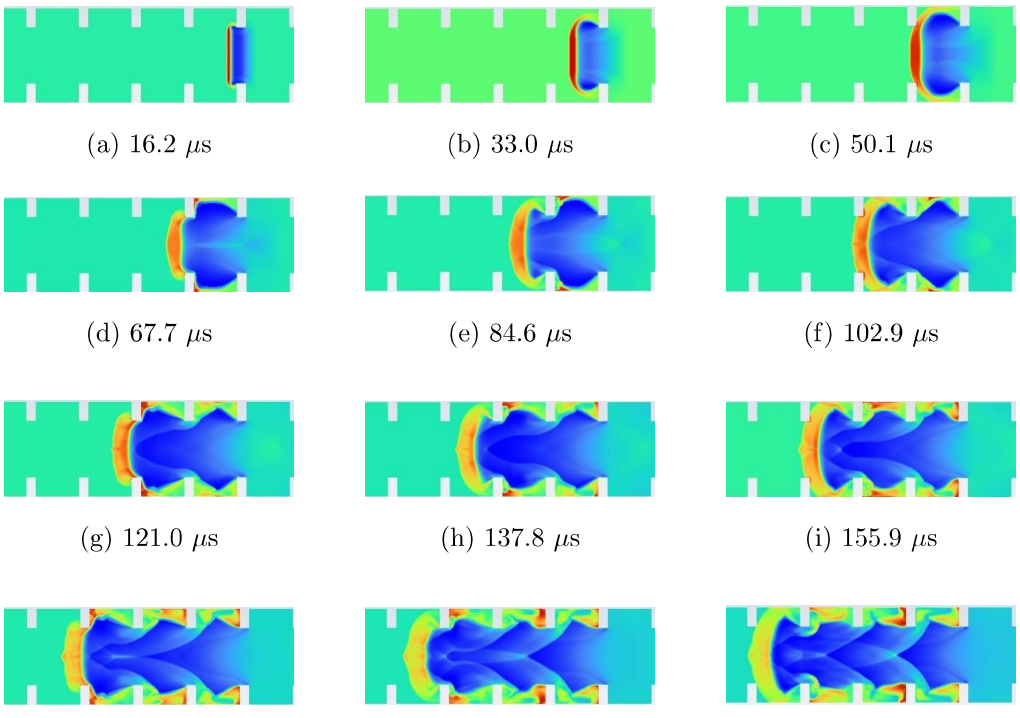

(a) 16.2 μs (b) 33.0 μs (c) 50.1 μs

(d) 67.7 μs (e) 84.6 μs (f) 102.9 μs

(g) 121.0 μs (h) 137.8 μs (i) 155.9 μs

(j) 174.7 μs (k) 193.0 μs (l) 211.3 μs

Figure 6.3: Sequential static temperature contours of shock wave transmission through baffles.

Two main waves develop after the lead shock wave hits a baffle: one that diffracts through the constriction and the other that creates a reflected shock wave off the baffle wall, forming an eddy within the baffle chamber due to flow separation. The reflected shock wave creates a high temperature pocket within the baffle chambers as can be seen beginning with Figure 6.3d. The process continues to repeat, where the lead shock wave rapidly expands then attenuates via transmission of each passing baffle, forming a complex system of oblique shocks within the core flow and converting axial momentum into radial momentum into the baffle chambers.

A further developed flow showing the static temperature contour aligned with the representative centerline temperature at 0.573 ms is shown in Figure 6.4. A semi-log scale is used for the temperature contour data for further distinction among the shock structure.

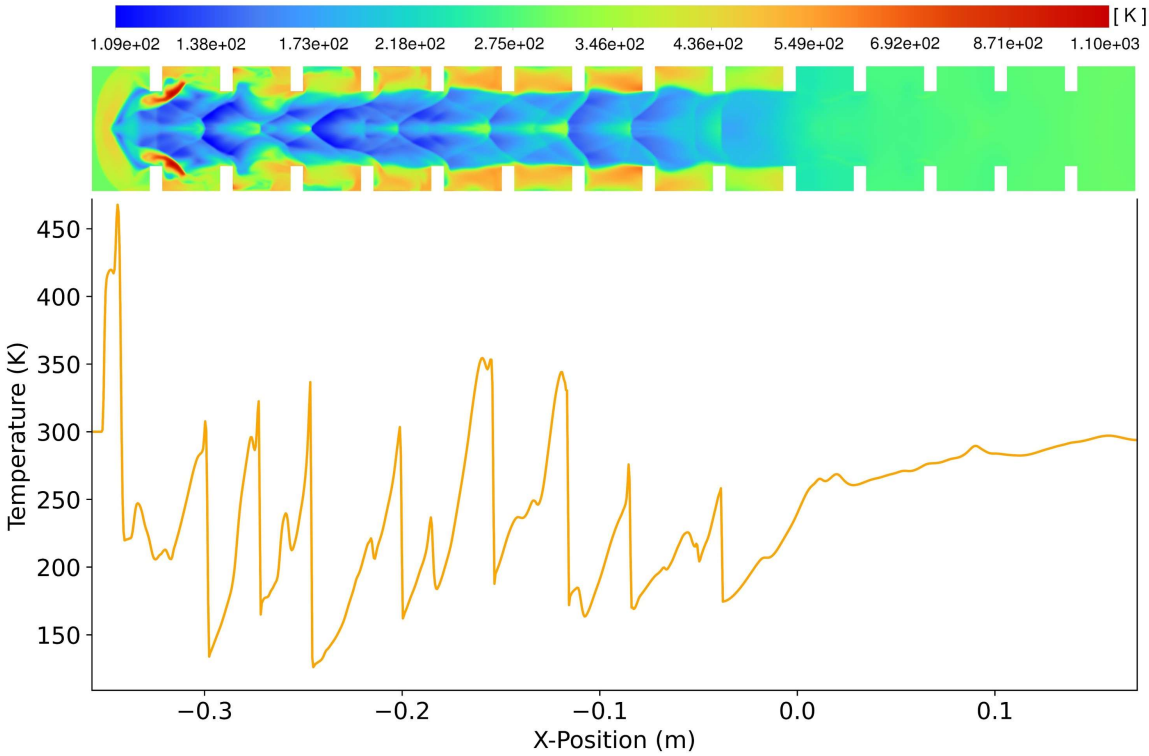

Figure 6.4: Centerline static temperature and semi-log profile contour CFD at 0.573 ms.

Several discontinuities in temperature exist due to the complicated reflected shock struc-

ture off the baffle walls. The centerline is the intersection point between reflected shocks and shows large fluctuations in temperature (∼150 K) due to those intersections and the expanding driver gas. As reflected shocks are infinitesimally small and on the order of only a few mean free paths thick, the distance between high and low temperature fluctuations are several orders of magnitude larger in the simulation due to the finite fidelity of the meshing. However, such differences are negligible when observing temperature trends on a macroscopic level.

The contact surface can clearly be seen by the steep increase in temperature close to the lead shock front. The contact surface also appears to have a differing wave motion than the lead shock wave when transmitting through the baffles. As mentioned, the lead wave shows spherical expansion into the increased cross-sectional area, while the contact surface and driven gas appear to punch through the baffles with a more linear chamber expansion, shearing past the eddies in the baffle chambers. As the driver gas continues to expand into the driven section, the shearing force between the turbulent eddies and core flow aid to the contribution of circulation. The developing relationship between the contact surface and lead shock front over the course of 60 baffles can be seen by the molar fraction of CO2 presented in Figure 6.5.

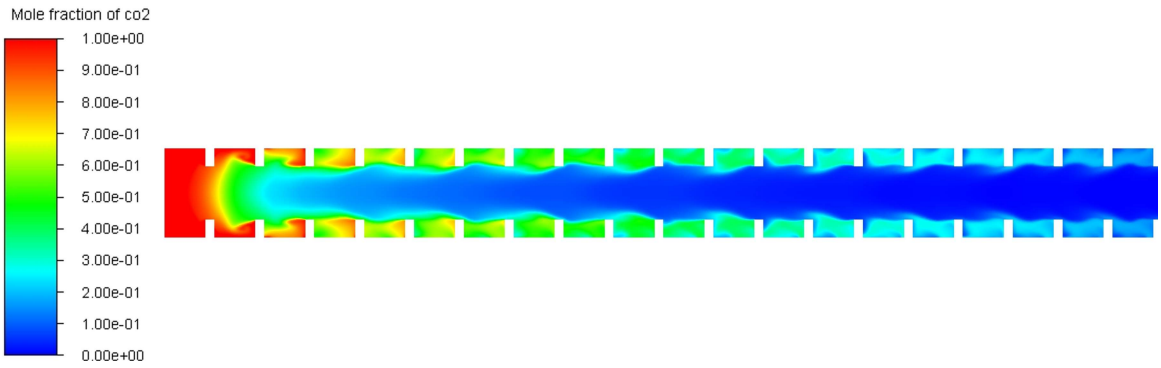

Figure 6.5: Molar fraction of CO2 vs. N2 after passage through 60 baffles (4.637 ms).

The contact surface after the passage of 60 baffles appears to smear between the driver and driven gases due to the complicated baffle interactions. The lead shock wave, although

not visible in the molar fraction graph, extends towards the end of the figure approximately one baffle further than the sharp gradient in molar fraction of CO2. Thus, the contact surface appears to be staying within two baffle lengths of the lead shock over the course of 60 baffles. This close relationship between the contact surface and shock front is unlike that of the smooth-bore shock tube case, in which the shock front develops significant distance between it and the contact surface over time. In both cases, the shock front creates increasing distance between it and the contact surface; however, in the baffled case, the constant lead shock wave attenuation appears to be limiting the increase in separation distance between the shock front and contact surface. Additionally, the contact surface distinctly separates the driven and driver gases in a smooth wall case, while the contact surface in the baffled case mixes the two gases as the wave progresses.

The static temperature profile over the course of 60 driven baffles is seen in Figure 6.6. The local fluctuations in temperature from the reflected shock wave interactions continue throughout the 60 baffle driven section. The average static temperature drops as the driver gas initially expands into the driver section, but continues with an upwards trend as the shock front is approached.

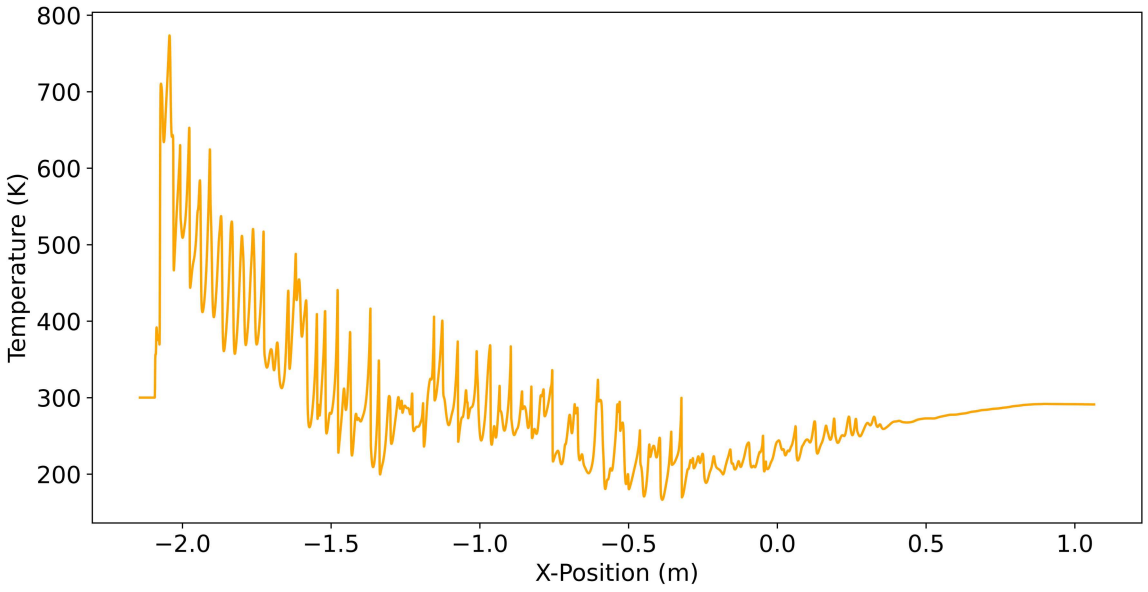

Figure 6.6: Centerline static temperature vs position at 4.637 ms.

This is a significantly different phenomenon compared to the smooth-bore shock tube case, where the temperature only decreases or remains constant until the shock-processed gas is reached. The increase in temperature among the expanding driver gas is likely a result from the baffle attenuation of the lead shock front and the continued heating of reflected shock-processed gas throughout the baffle chambers.

The particle velocity magnitude contour aligned with the representative centerline velocity at 0.573 ms is shown in Figure 6.7. Similar to the static temperature, the particle velocities show drastic fluctuations of several hundred meters per second. The large fluctuations appear to be specifically in stagnation points along the centerline, where the particle transmission lines from the reflected shocks intersect and reflect back towards the baffle chambers.

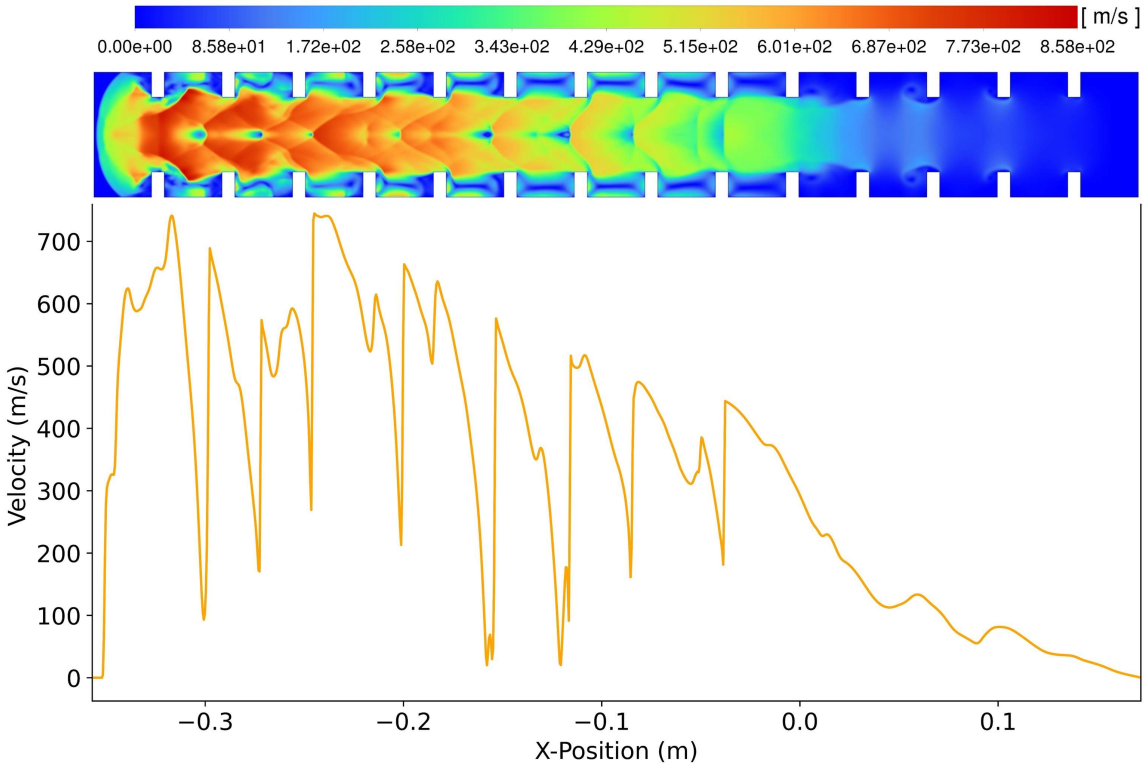

Figure 6.7: Centerline velocity magnitude and profile contour CFD at 0.573 ms.

Directly behind the shock front yields an interesting phenomenon, in which the imme-

diate shock-processed particle velocity is less than that of the expanding driven and driver gas in the baffles behind. Particle velocity vectors in the chambers can be seen in Figure 6.8. Due to no inflation being used along the wall boundaries in the mesh, the boundary layer development within each chamber is likely poorly defined. However, the macroscopic behavior can still be observed. The particle velocities circulating in the chambers are typically several hundred meters per second slower than the core flow punching through the chambers and change over time, eventually becoming stagnant due to viscous dissipation.

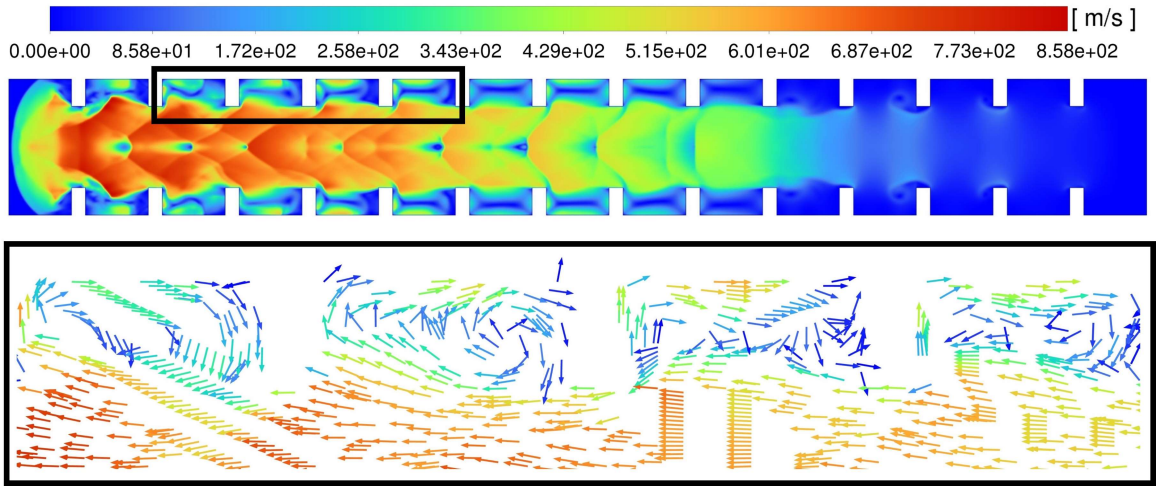

Figure 6.8: Velocity magnitude vector plot at 0.573 ms.

The centerline axial particle velocity profile over the course of 60 driven baffles is seen in Figure 6.9. The average particle velocity shows a decrease in magnitude from the shock front to the driver section in a similar manner to Figure 6.8. As the CFD results, experimental data, and hand calculations based on picture outputs and timestamps indicate the lead shock is propagating around ∼400 m/s to ∼500 m/s after passage through 60 baffles, the same interesting phenomenon is shown in which the particle velocity in the expanding driver and driven gas (500 m/s to 700 m/s at its highest) becomes greater than the lead shock propagation velocity itself. The phenomenon can further be seen by looking at the transient particle velocity towards the end of the shock tube in Figure 6.10.

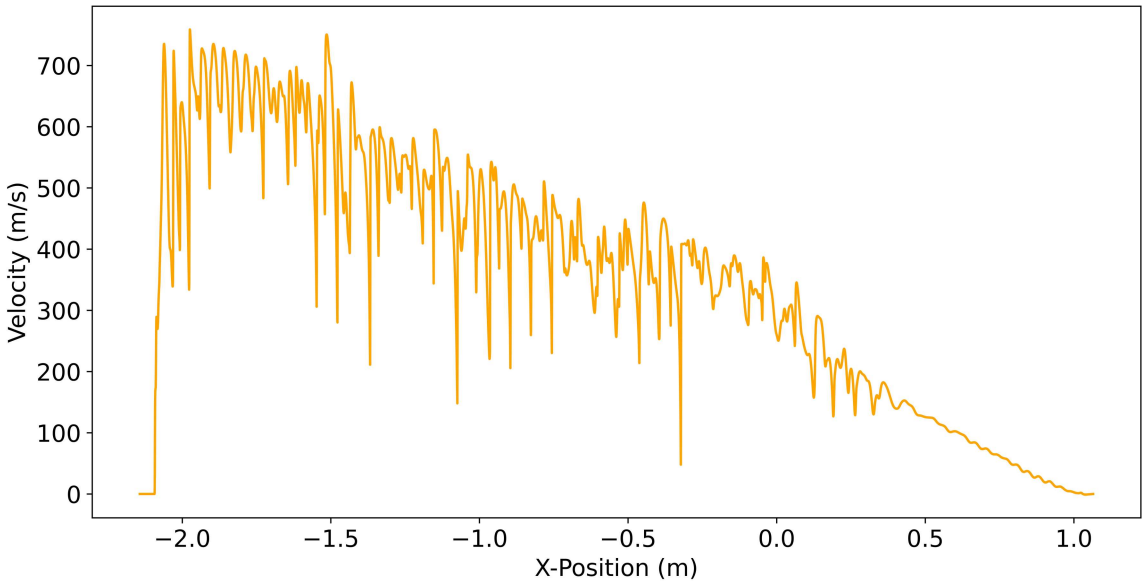

Figure 6.9: Centerline axial velocity vs. position at 4.637 ms.

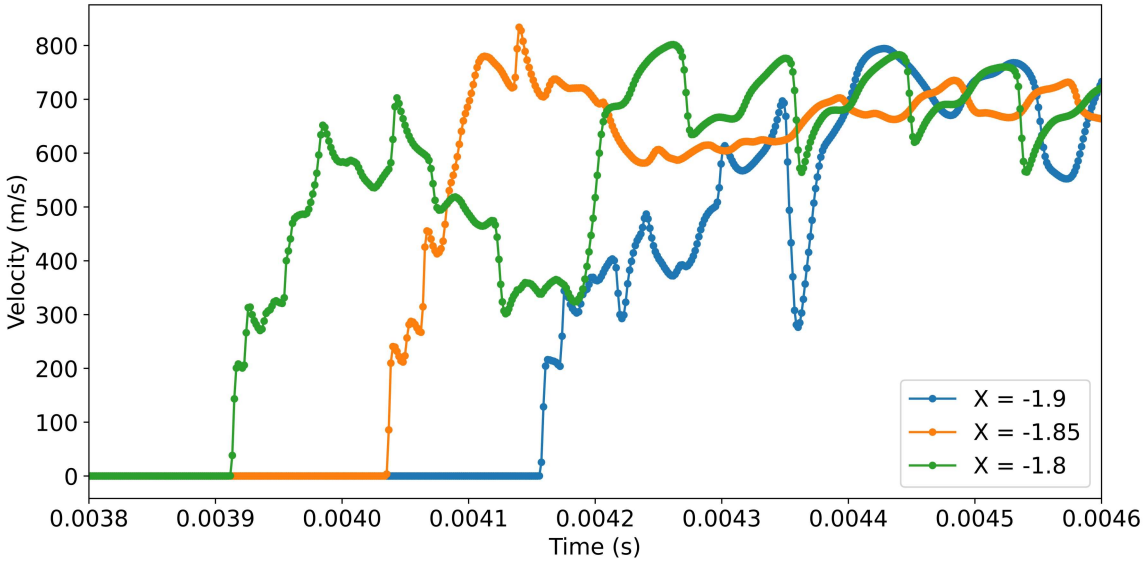

Figure 6.10: Transient axial velocity along the centerline at three locations.

The exact circumstances causing such results is unknown; however, the driven and driver gases appear to be expanding into the baffle chambers then accelerating back through each baffle constriction at an increased velocity, creating a throttling effect. Reflected shock interactions from the baffles could also be a contributing factor in particle acceleration. Overall, the high velocity gases do not appear to overtake the lead shock as the energy dissipates into the baffle chambers. The particle velocity directly behind the shock front could also potentially be an appropriate velocity match to that of the shock strength before it gets accelerated, as can be seen by the initial steps in velocity in Figures 6.7, 6.9, and 6.10.Further investigation into the gas dynamics of shocks through baffles should be included in future work, as numerical error could potentially be artificially inflating the particle velocity values and greater mesh and timestep resolution should be explored. However, the increased particle velocity by the expanding driver and driven gases as shown could provide significant benefits towards low velocity start.

The Mach number contours presented in Figure 6.11 with the centerline values over 60 baffles are as shown in Figure 6.12. These contours show flow that perturbations after the lead shock front passes begin to decay and leave only weak shocks remaining in the free stream. The density contour aligned with the representative centerline density at 0.573 ms is shown in Figure 6.13 with the centerline over 60 baffles in Figure 6.14 A semi-log scale is used on the contour for further distinction among the shock structure. The density contours show the same flow shock structure off the baffle walls with a fluctuating density along the centerline and smoothly decreasing density average as the shock front is approached.

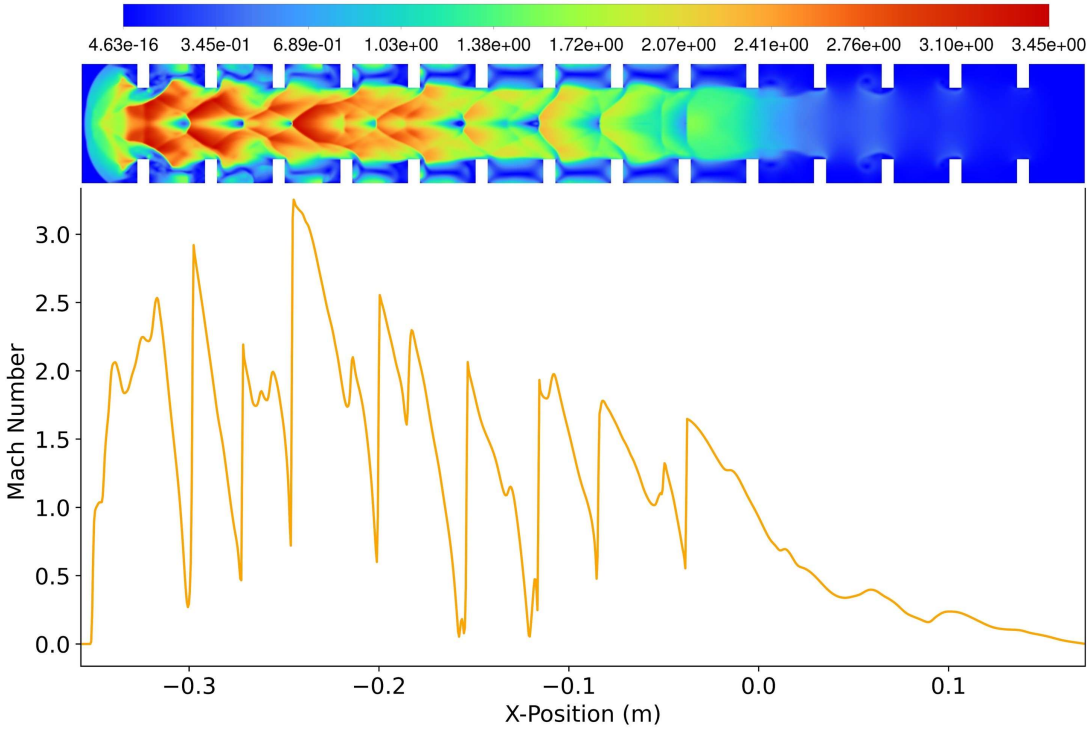

Figure 6.11: Centerline Mach number and profile contour at 0.573 ms.

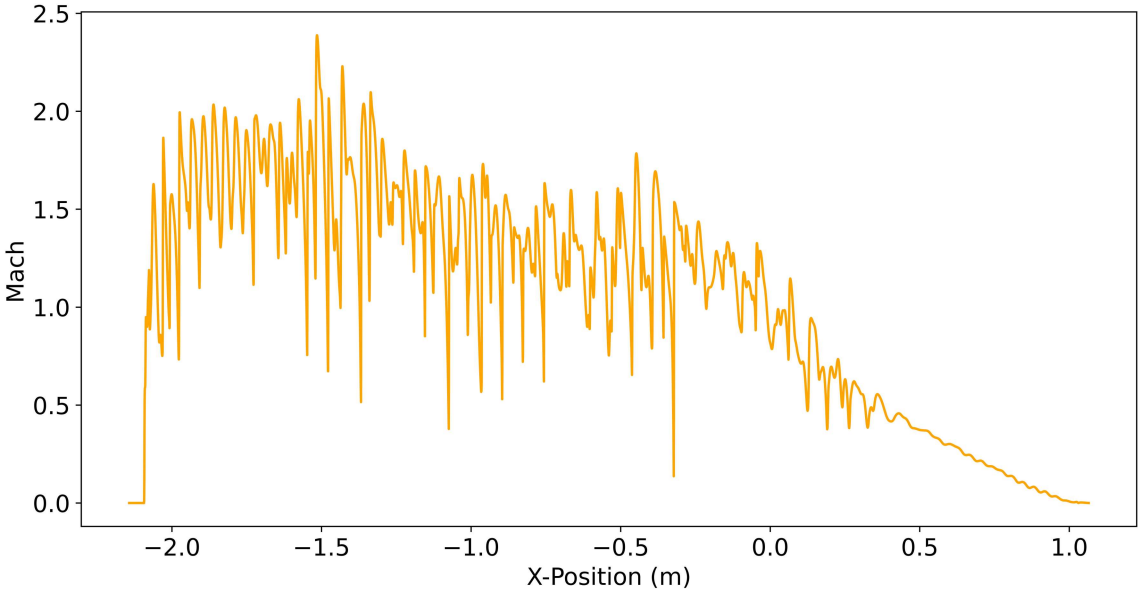

Figure 6.12: Centerline Mach number vs. position at 4.637 ms.

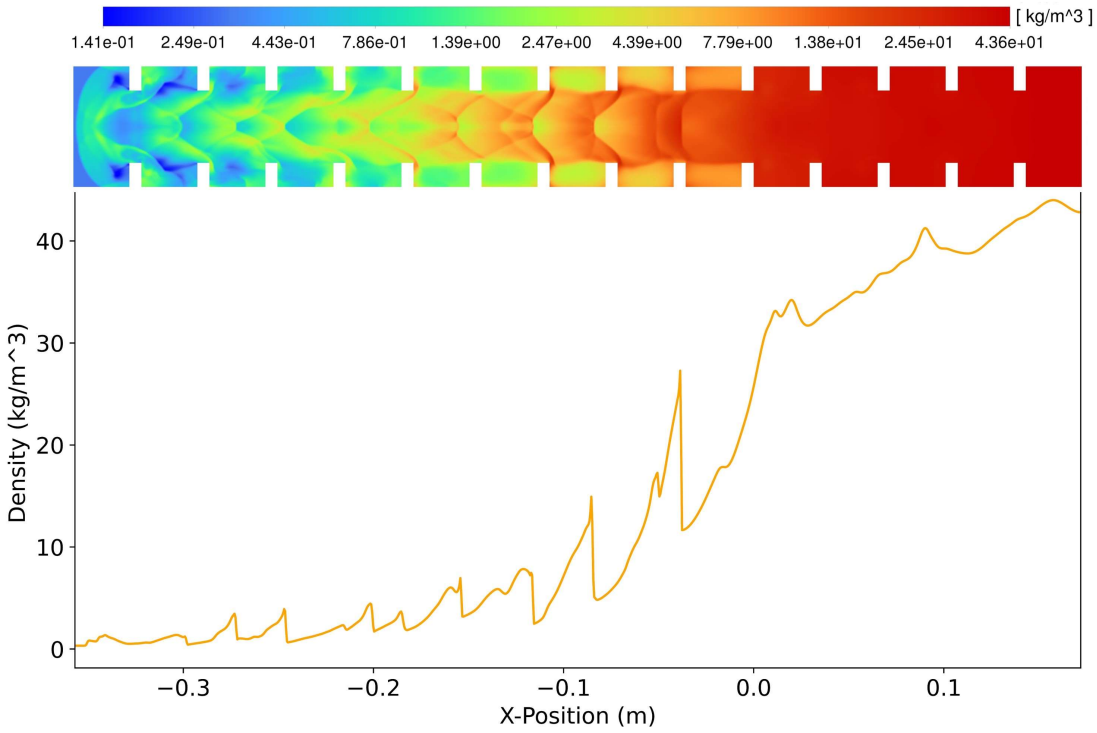

Figure 6.13: Centerline density and semi-log profile contour at 0.573 ms.

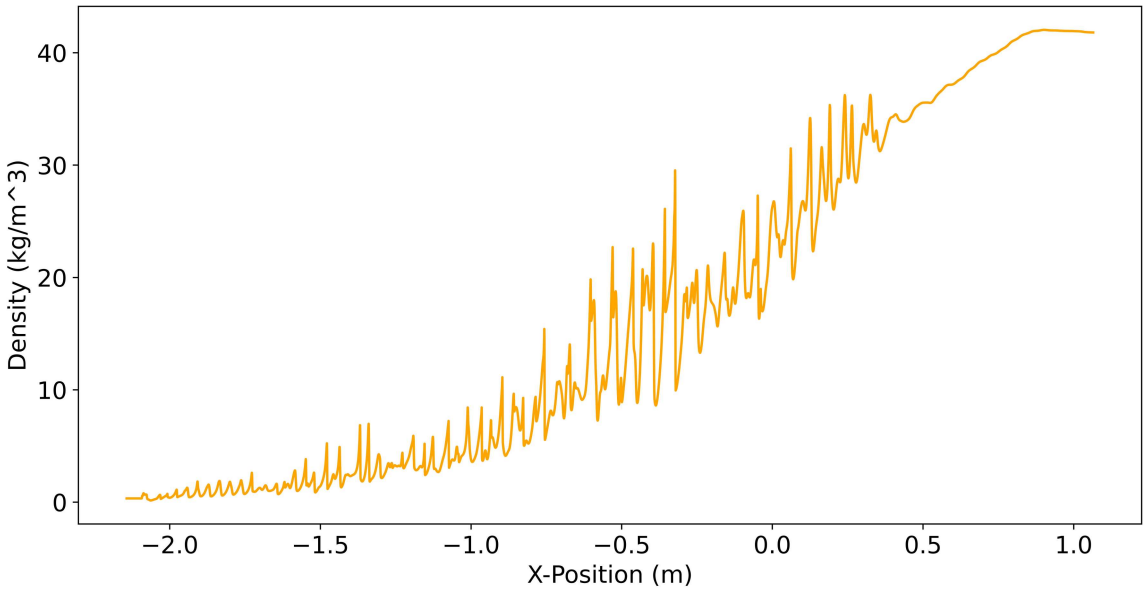

Figure 6.14: Centerline density vs. position at 4.637 ms.

Finally, the centerline total pressure is presented at four different timestamps approximately corresponding to the location of the experimental pressure transducers in Figure 6.15. The total pressure rise after the lead shock front passes decreases as the shock transmits through an increasing number of baffles. The total pressure loss over successive timestamps is unlike that of the ideal smooth-bore shock case, where the total pressure increase after the shock front is the same regardless of how far the wave has traveled. The total pressure loss in the case of a baffled shock tube is due to the non-isentropic shock and reflected shock effects occurring off the baffle chambers, viscous effects turning kinetic energy into heat, and flow separation. The total pressure loss can be seen as a result of the weakened shock strength from the lead shock transmitting through successive baffles.

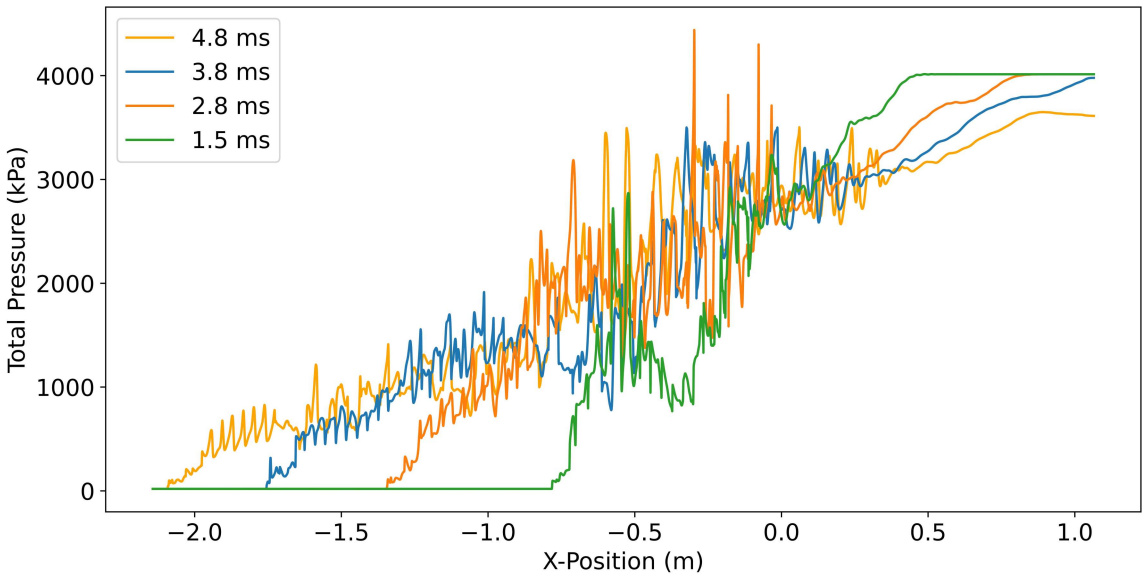

Figure 6.15: Centerline total pressure vs. position at four timesteps.

6.3 Chamber Wall Pressure

Temporal profiles of the pressure traces experimentally obtained at four locations in the driven tube are compared with CFD tube-wall pressure histories in Figures 6.16, 6.17, 6.18, 6.19. The entirety of the simulation data after the passage of each pressure rise is shown, thus each graph is presented on the same representative time scale showing the passage of the wave. As the lead shock propagation velocities for the experimental data and CFD were different, the CFD pressure data at each respective location was aligned to that of the experimental data. The raw experimental temporal pressure data was converted to engineering units using factory calibrations and capacitance of the transducer itself, the in-line charge converter, and the connecting cable. Note that the same calibration was applied to each transducer based on a generic sample mean of $\bar{x} = 12362$ psi/volt ($\sigma = 262.9$ psi/volt). Furthermore, a fast Fourier transform was ran on each signal to determine and zero out the DC offset before aligning it with the quasi-static driven fill pressure.

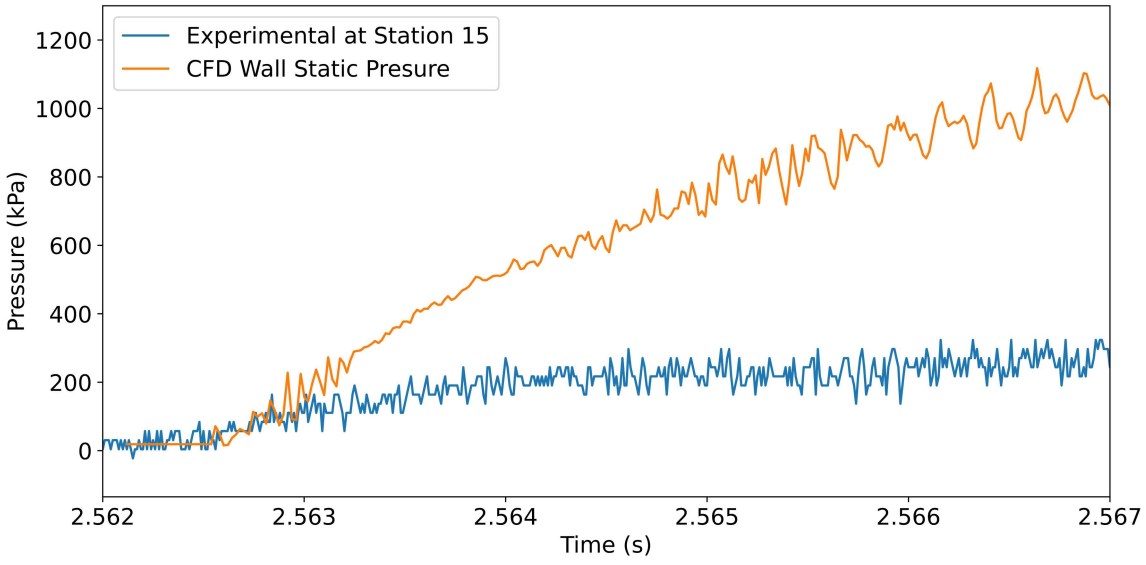

Figure 6.16: Laboratory pressure transducer vs. CFD at X=-0.227 m from the diaphragm.

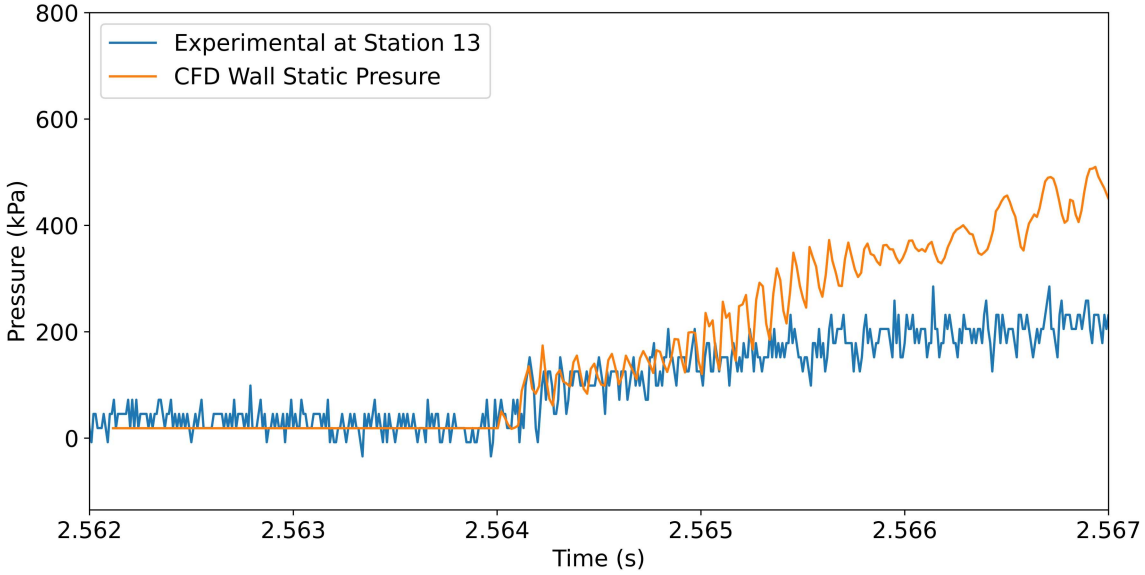

Figure 6.17: Laboratory pressure transducer vs. CFD at X=-0.941 m from the diaphragm.

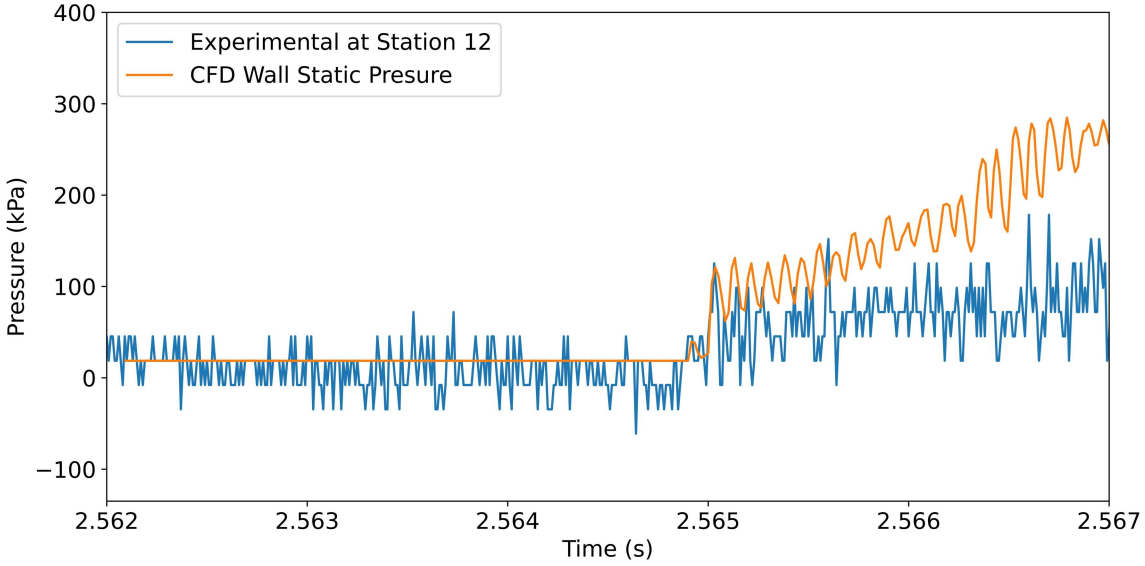

Figure 6.18: Laboratory pressure transducer vs. CFD at X=-1.298 m from the diaphragm.

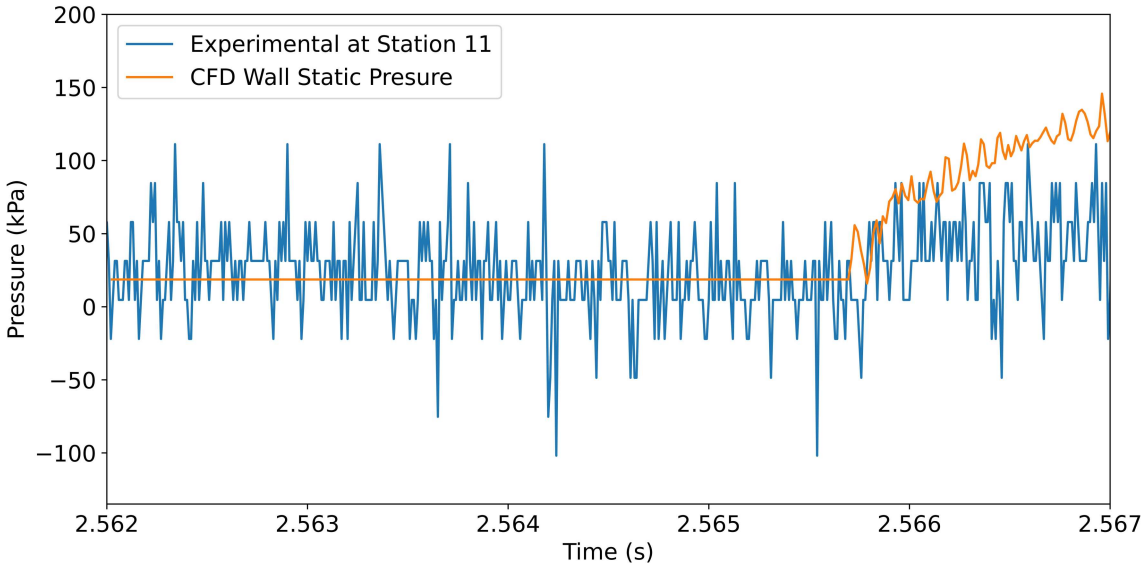

Figure 6.19: Laboratory pressure transducer vs. CFD at X=-1.655 m from the diaphragm.

The magnitude of the lead pressure spike due to the passing shock wave in the CFD simulation is within ∼15% (12.5 kPa) of the experimental data at each instrumentation station. Although the lead spike magnitudes are similar for both cases, the CFD simulation shows an increased rate of pressure rise after the lead shock wave passes compared to the laboratory transducers. Zoomed out figures of the same four pressure history graphs are presented in Figure 6.20.

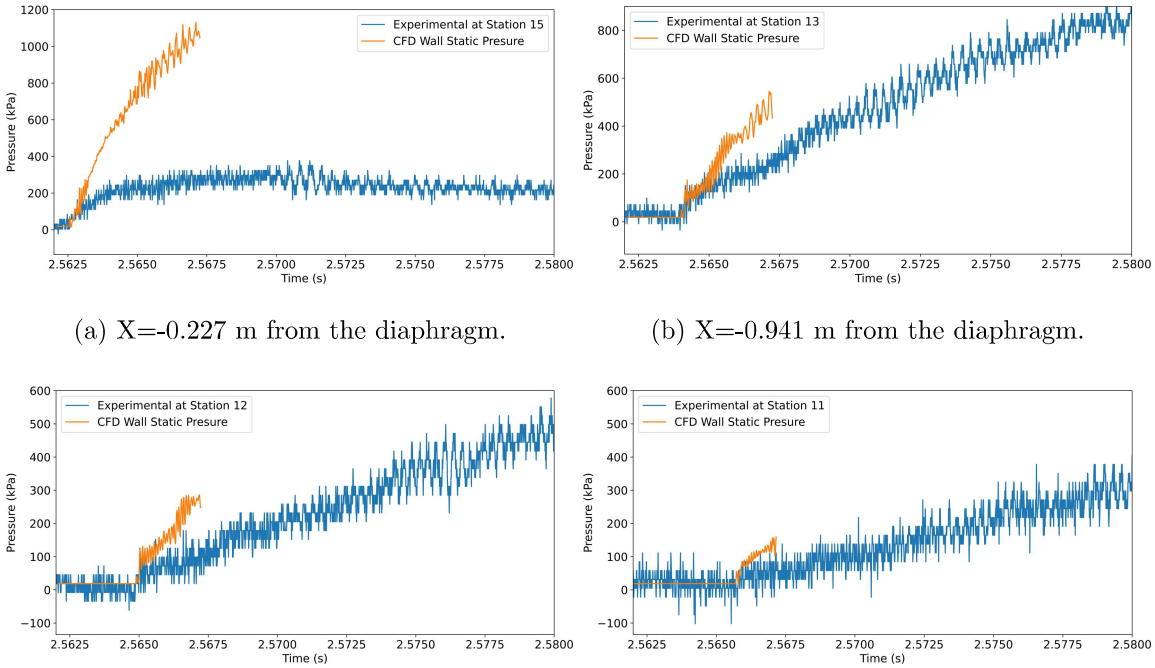

(a) X=-0.227 m from the diaphragm.

(b) X=-0.941 m from the diaphragm.

(c) X=-1.298 m from the diaphragm.

(d) X=-1.655 m from the diaphragm.

Figure 6.20: Laboratory pressure transducer vs. CFD wall pressure.

The laboratory pressure transducer at station 15 (Figure 6.20a) was found to have a known error in its outputted magnitude and thus can be disregarded from the analysis. The pressure rise seen in the CFD simulation eventually occurs in the experimental pressure data, but at a delayed time. Additionally, after a somewhat smooth oscillating pressure waveform in the CFD, a stepped waveform with several smaller frequencies appears. A similar waveform also develops in the experimental data at a delayed time. The described developed waveform is presented in Figures 6.21 and 6.22.

Note the two figures are not directly comparable, as they are taken from different locations in the tube at different timesteps and hence at different particle velocities; thus, the primary purpose is to show the similar waveform that develops in both the laboratory transducers and in the CFD data. The CFD simulation is presented on a smaller timescale due to the finite simulation time. Simple calculations modeling the BTRA 501 baffle insert as a

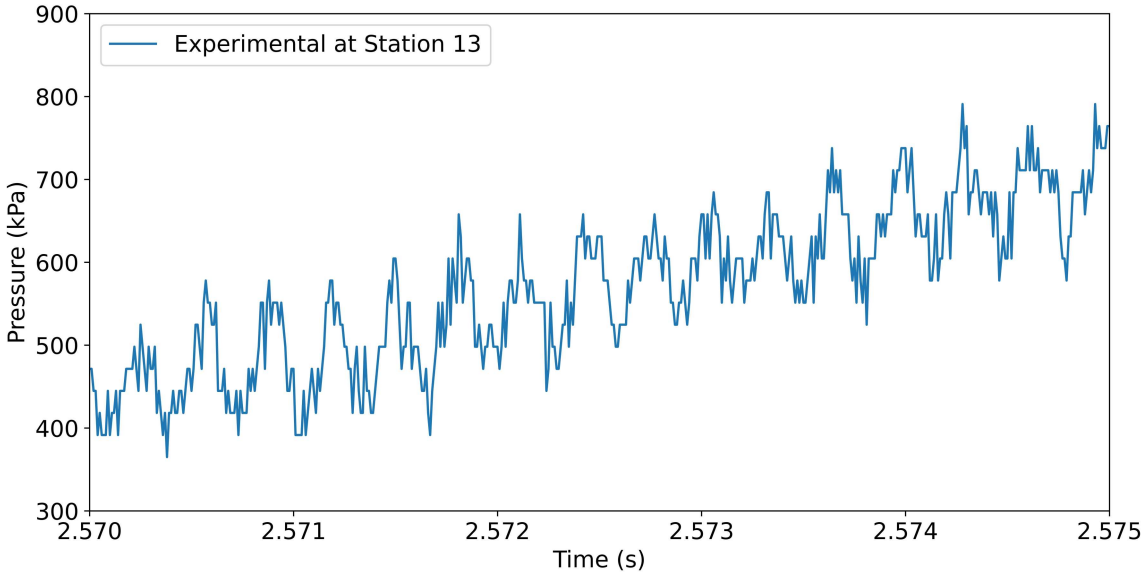

Figure 6.21: Laboratory transducer waveform at X=-0.941 m from the diaphragm.

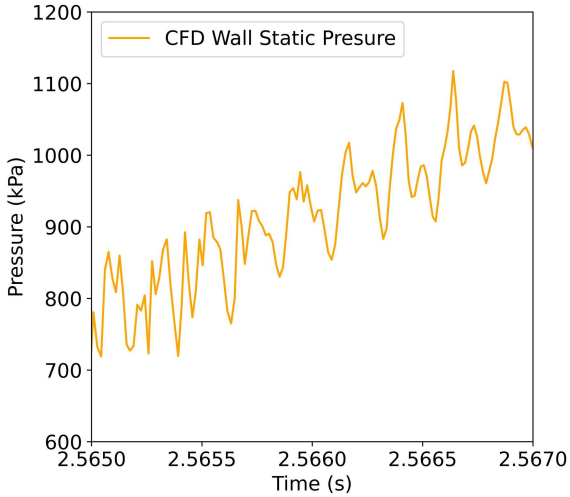

Figure 6.22: CFD waveform at X=-0.227 m from the diaphragm.

Helmholtz resonator outputs a resonant frequency of ∼2500 Hz in nitrogen, corresponding to a wave period of 0.4 ms, similar to what is seen in the outputted data. The oscillatory waveform begins to develop after the contacts surface has passed and overall may be an effect of the expanding driver gas throttling through each of the baffle constrictions. The magnitude of the oscillations is consistently around 180 kPa for both the laboratory and CFD results.

Important to note is the experimental data were collected at the resolution limit of the pressure transducers; the transducers are rated to 100 ksi and are attempting to capture initial pressure spikes on the order of ∼25 psi (180 kPa) or less. Due to the recessed mounting of the pressure transducers, the expanded shock at the tube wall also does not directly hit the face of the transducer. The shock diffracts through the recessed area at the instrumentation port then induces a reflected shock off the wall before reaching the instrumentation face. Therefore, the pressure measurements at the low range of the transducer ultimately leave an undetermined time history of pressure rise. Additionally, the CFD results only offer finite fidelity in its solution, largely due to the 0.5 mm element size and no refined mesh inflation along the wall boundary to capture the pressure gradient with greater accuracy.

Despite the difference in pressure rise, each transducer displays a gradual pressure increase after the initial shock, and a decreasing step pressure magnitude as the shock travels further in the tube. The decrease in pressure amplitude after each passing baffle is yet another metric showing shock attenuation.

Chapter 7

EXPERIMENT DESIGN

Experiment design for low velocity start (including proposed tube configurations, propellant chemistries, entrance velocity, and order of operations) is outlined to test ignition and sustained projectile starting based on the preliminary results.

7.1 Synopsis

The low velocity start technique involves accelerating propellant towards an oncoming ram accelerator projectile to reduce the burden of start gun velocity. The high Mach number expanding flow is most easily created by a shock tube, in which a diaphragm separating propellant mixtures at a pressure differential bursts and accelerates the propellant towards the projectile. An example of the transient interaction between the projectile and shock tube gas dynamics is as follows:

1. A shock tube is partitioned with an entrance diaphragm, a double-diaphragm configuration between regions one and four (driven and driver sections), and an exit diaphragm entering a ram stage.
2. The projectile is launched by a start gun and the double-diaphragm configuration bursts at a prescribed delay time.
3. The projectile reaches the entrance diaphragm of region one before the lead shock reaches the same entrance diaphragm.
4. Combustion is initiated in the quiescent propellant of region one, establishing the thermally choked propulsive mode.
5. The projectile accelerates supersonically and encounters the lead shock wave, swallowing the shock and remaining gas dynamically started.
6. The projectile continues to supersonically accelerate through the shock heated gas and

encounters the contact surface with an impedance mismatch.
7. The projectile remains started after reaching the driver propellant past the contact surface and accelerates with increased thrust due to higher density.
8. Acceleration begins to rapidly increase as the density increases throughout the driver's expansion fan, until eventually the projectile overtakes the rear expansion wave and enters a region of constant density.
9. The projectile eventually exits the driver through a diaphragm and enters a quiescent propellant mixture for traditional ram acceleration.

Despite the significant benefits offered by implementing the low velocity start solution, several challenges must be overcome involving the complex gas dynamics of the proposed system. Thus, the system must be experimentally tested to verify feasibility and establish proof of concept. The work in this thesis outlines an experimental design to test those challenges.

7.2 Test Configuration

The 8-m-long test section at the ram accelerator facility will be used for testing of the baffled shock tube coupled ram system. The test section will be converted solely into a shock tube, with the beginning 6 m (BT1, BT2, and BT3) being the driven section and the remaining 2 m (BT4) being the driver section. BT3 and BT4 will be separated by a custom double-diaphragm insert, similar to that in section 4.1, with the exception that the insert will be large enough to accommodate two BTRA 501 baffle inserts. The same baffle insert configuration shall be used as that in Figure 3.4, with the exception that any BTRA 501 and BTRA 501s inserts can be interchanged with one another.

Propellant combinations are chosen for the driver and driven sections based on robust propellant combinations experimentally verified in traditional baffled tube ram acceleration by researchers at the University of Washington. However, ignition of the propellants have not been confirmed or previously tested when used in the baffled shock tube configuration proposed. Several factors may make ignition and continued combustion difficult, including the low driven pressure and the low temperature of the expanding gases from the driver.

Thus, demonstrating successful ignition of the propellant and a continued started propulsive mode throughout the entirety of the shock tube is a key goal from this experiment.

The results from the experimental pressure ratio investigation indicated a pressure ratio of ∼215 may have the necessary particle velocity in order to be beneficial for low velocity start. A methane-oxygen with carbon dioxide diluent propellant with molar ratios of $1CH_4+2O_2+2CO_2$ (313 m/s) will be used in the driven section at 2.7 psia to 3.3 psia (fill to the low side, as the driven section pressure will increase due to leaks in the system as the double-diaphragm and driver sections are filled). Carbon dioxide was chosen as a diluent due to its low sound speed, ultimately raising the propagating shock Mach number from the expanding gases and thus lowering the required entrance velocity from projectile. A robust methane-air-oxygen propellant combination with molar ratios of $1CH_4+2O_2+4.67N_2$ (353 m/s) and an equivalent ratio of one will be used in the driver section at 650 psia to 700 psia. The propellant mixture corresponds to a blended 30% oxygen 70% nitrogen enriched air. The same propellant in the driver section will be used in the double-diaphragm section at an intermediary pressure of 150 psia to 250 psia (fill to the low side, as the double-diaphragm pressure will continue to increase as the driver is being filled). The $1CH_4+2O_2+2CO_2$ propellant may also be a suitable alternative for the driver. The overall proposed fill pressures give a pressure ratio range of 197-260 between the driver and driven sections.

The pressure ratio investigation indicated shock strength was highly dependent upon the quality of diaphragm opening, and thus the following Mylar diaphragm configuration is proposed. Note the configuration was not tested and is an estimate based on experimental results that may require iteration. One 0.381 mm (0.015") diaphragm will be placed at the entrance of BT1, and one 0.381 mm stacked with one 0.254 mm (0.010") diaphragm will be placed at the exit of BT4. The entrance and exit diaphragm's sole responsibility are to hold the pressure differential for each fill pressure in the shock tube, with the entrance diaphragm also needing to be able to prevent pre-mature bursting due to blow-by gases from the start gun. Two 0.127 mm (0.005") diaphragms stacked together will be placed at the end of BT3 (on the driven side of the double-diaphragm insert). One 0.381 mm diaphragm with one 0.127 mm diaphragm stacked on top scored together at 850 psig in an 'x' configuration will be placed on the other side of the double-diaphragm insert (beginning of BT4). The scored

side will be placed upstream facing the driver.

7.3 Entrance Velocity

The starting process for the ram accelerator can lead to a variety of different outcomes: successful start, sonic diffuser unstart, wave fall-off, and wave unstart [8]. The minimum entrance velocity is determined by a combination of the propellant composition and geometric throat ratio such that the Mach number at the projectile throat is greater than one [6]. So far, theoretical and computational analyses for the starting process have been inadequate in determining accurate starting envelopes, and thus experimental investigations have defined successful operating envelops as a function of the projectile Mach number and heat release of the mixture [4, 8]. However, an approximation using isentropic compression based on the projectile throat area, tube bore area, and ratio of specific heats gives the determined sonic diffuser unstart Mach number as [38]:

$$\frac{A_{tube}}{A_{throat}} = \frac{1}{M_{sdu}} \left(\frac{\frac{\gamma+1}{2}}{1 + \frac{\gamma-1}{2} M_{sdu}^2} \right)^{\frac{\gamma+1}{2(1-\gamma)}} \tag{7.1}$$

The sonic diffuser unstart Mach number is the minimum Mach number necessary for starting at the defined geometry ratio. At the same projectile throat area in the SBRA case, the BTRA utilizes the chamber diameter of the baffle to represent the effective tube area, resulting in a reduced sonic diffuser unstart Mach number and thus lower required entrance velocity for successful start at the same heat release. The methane-air-oxygen propellant recommended in the driven section for this experiment has demonstrated entrance velocities as low as 700 m/s for smooth acceleration in the BTRA [29]. The methane-oxygen with carbon-dixoide diluent propellant in the driven section has demonstrated entrance velocities as low as 600 m/s when starting in the BTRA 111 baffle inserts in Figure 3.3c [39].

The particle velocities as indicated by the CFD in Figures 6.7 and 6.9 and their effective influence on a successfully started ram accelerator projectile remain undetermined, as the results indicate the particle velocity may fluctuate several hundred meters per second along the centerline. Additionally, unlike in the smooth-bore shock tube case, the particle velocity in regions two and three of the baffled shock tube are not constant, but rather vary along the

length of the tube. The maximum particle velocity in the tube also remains undetermined as discussed by the particle velocity accelerating greater the lead shock propagation velocity in the CFD results. The simulation was also based on the BTRA 501 baffle insert geometries, while experimental results indicated further reduction in shock strength in the larger chamber diameter BTRA 111 inserts compared to the BTRA 501 inserts. This increase in chamber diameter will likely result in further decrease particle velocity, subtracting from the benefit for LVS. All of the mentioned components leave questions on the magnitude of useful gas acceleration towards the oncoming projectile. However, no distinct limit exists at which the low velocity start concept is no longer beneficial to reducing entrance velocity. The overall reduction of the projectile's entrance velocity will only increase or decrease depending on the resultant particle velocity in the shock tube, and there is no upper Mach number limit on the required entrance velocity for successful start. Therefore, the proposed entrance velocity of the projectile is only an estimation and will likely require iteration. A conservative estimate is provided based on the low particle velocity range in the CFD results and a factor of safety of two.

When comparing the CFD particle velocity results after the shock front travels 0.35 m vs. 2 m, the average particle velocity spans approximately 200 m/s to 450 m/s and 200 m/s to 600 m/s respectively (excluding the expansion fan in the driver). As the minimum velocity for both the 0.35 m and 2 m cases were approximately the same, the minimum velocity will assumed to be 200 m/s regardless of how far the shock front travels in the baffled tubes. Thus, 100 m/s (200 m/s at a FOS = 2) can be subtracted from the required projectile entrance velocity. As the projectile needs to remain started through the methane-air-oxygen propellant in the driver section (which requires the higher starting Mach number), the gas particle velocity from the shock tube will be subtracted from the minimum entrance velocity of 700 m/s, giving an estimated projectile entrance velocity of 600 m/s or greater.

Another challenge may be the projectile traveling through the low particle velocity propellant in the driver section of the shock tube, depending on the timing of projectile hitting the expansion wave and its reflection off the exit diaphragm. In this case, the reduced Mach number of the flow may cause wave unstart and thus require a higher entrance velocity. However, if successful ignition occurs and the thermally choked propulsive mode is established

and maintained throughout the test section, a sweep in entrance velocity can be conducted to determine the minimum necessary entrance velocity for the conditions outlined.

The proposed projectile and obturator are commonly demonstrated in successful BTRA operation at the propellants of interest. The axisymmetric one piece polycarbonate projectile and polycarbonate obturator are represented in Figure 7.1.

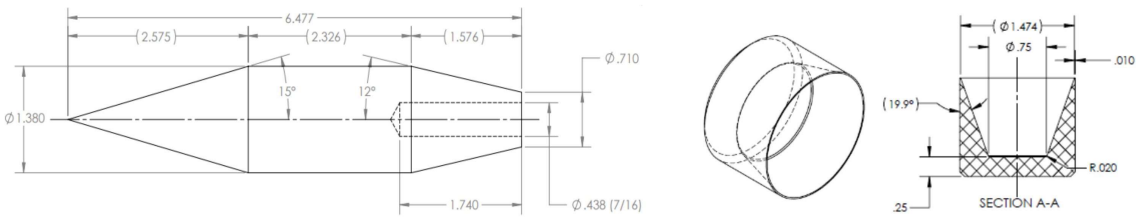

Figure 7.1: P380-1.7BL Projectile and Obturator 101 for the experiment (dimension in inches).

7.4 Timing and Jitter

The timing between projectile launch and the double-diaphragm configuration bursting is crucial for the projectile to hit the wave in the test section and thus must be quantified in order to establish order of operations. Several timestep estimates will therefore be made based on analytical calculations and experimental data. Uncertainties of the timestep estimates for each action will be reduced with further calibration when conducting the experiment.

When conducting the controlled diaphragm bursting tests in Section 4.1, data was collected on the delay from the signal to the solenoid of the needle valve to when the upstream driven diaphragm burst. The waveform of the of the battery triggering the solid stay relay and the estimated locations of triggering are shown in Figure 7.2. The time difference between the earliest and latest estimated trigger timestamps is consistently 0.8 $\pm$ 0.05 ms across each test series.

The controlled diaphragm burst test series utilized a nitrogen smooth-bore driver section with and piezoelectric pressure transducers to track the velocity of the expansion fan. The results from three separate tests and seven total velocity measurements at varying locations

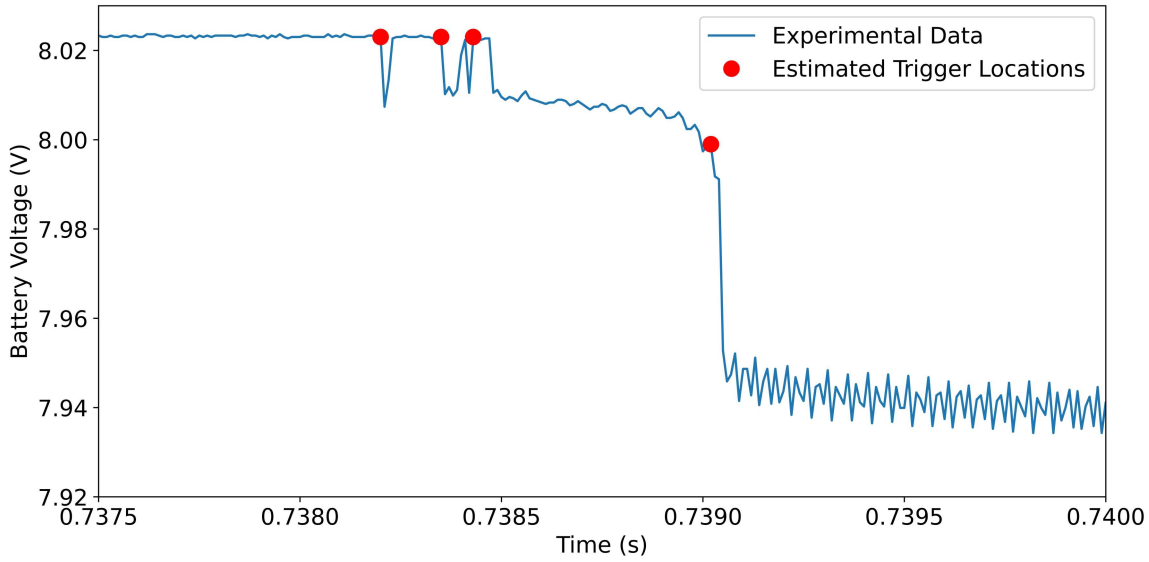

Figure 7.2: Trigger voltage waveform and estimated trigger timestamps.

in the driver tube indicated the expansion fan was traveling at a sample mean of $\bar{x} = 350.9$ m/s ($\sigma = 10.8$ m/s), a less than 1% difference compared to the theoretical sound speed of nitrogen. The wave travel time between the upstream diaphragm and location of the first pressure transducer was calculated based on the sound speed of nitrogen and the distance between the diaphragm and sensor. The wave travel time and initial trigger timestamp was then subtracted from the timestamp of the first expansion wave to give a delay from the signal to when the upstream diaphragm bursts.

The delay from the four estimated trigger timestamps in Figure 7.2 were averaged for each test and plotted against the test's respective pressure ratio as shown in Figure 7.3. A power trend line was fit to the data points and a new estimated trigger delay based off the pressure ratio range of 197-260 as outlined in subsection 7.2 results in a delay between 175-183 ms.

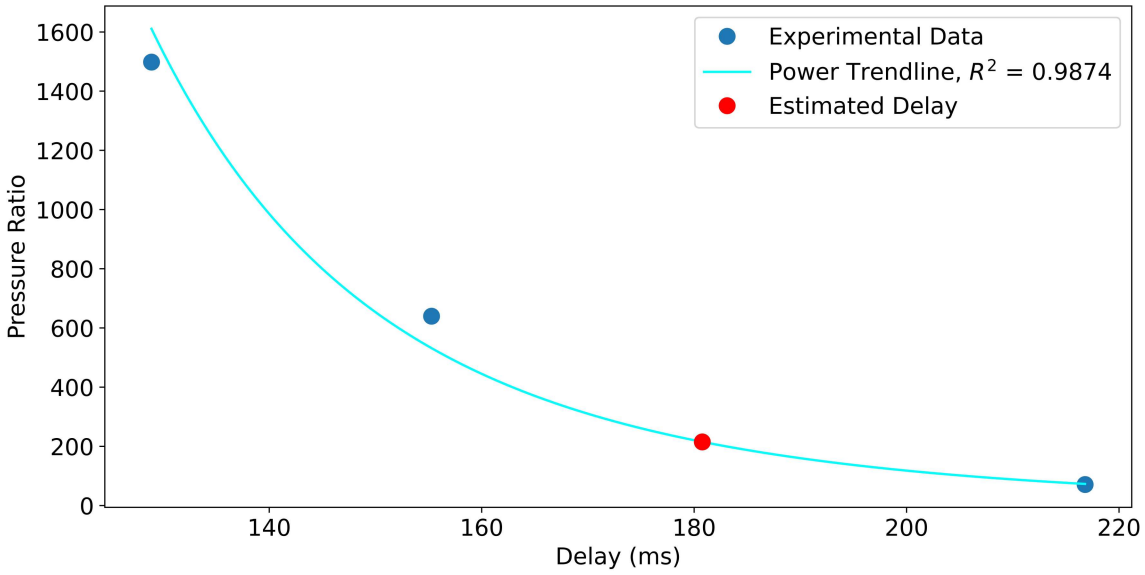

Figure 7.3: Driver/driven pressure ratio vs. delay in milliseconds from the signal being sent to the needle vale and the upstream diaphragm bursting.

The results from the test configuration presented in Figure 6.1 will be used to estimate the total wave transit time across BT3, BT2, and BT1. Transit time through tube BT3 is based on a combination of the experimental $\triangle t$ across five instrumentation stations and the last average velocity data point used as an average to estimate the remaining baffle transit time. Both the CFD and experimental data indicate a drastic drop in shock strength initially before approaching a leveled "steady state" velocity. The "steady state" velocity at the end of BT3 will then be used as the approximate wave transitioning velocity through BT2. BT1 contains BTRA 501 baffle inserts along with BTRA 111 baffle inserts and the experimental data will be used to estimate the transit time through BT1 in the same manner as that of BT3.

The total transit time from the signal being sent to the solenoid to the wave reaching the entrance diaphragm of BT1 is estimated in Table 7.1.

Action	$\triangle t$ (ms)	Total Time (s)
Signal sent to the needle valve solenoid	0	0
Upstream diaphragm bursts	175 - 183	0.175 - 0.183
Wave reaches end of BT3	5	0.180 - 0.188
Wave reaches end of BT2	6	0.186 - 0.194
Wave hits entrance diaphragm in BT1	14	0.200 - 0.208

Table 7.1: Estimated time budget for the shock wave to reach the entrance diaphragm upon the signal first being sent.

The gas gun in the ram accelerator facility will be used to launch the projectile up to its entrance velocity. The gun will be configured to operate in a controlled manner using a similar interdiaphragm configuration to expand the gasses and accelerate the projectile through the launch tube. A ball valve is used instead of a needle valve to equalize the breech and interdiaphragm pressures, and aluminum diaphragms are used instead of Mylar. The ball valve solenoid will be triggered by a switch and solid state relay similar to that in the initial controlled diaphragm burst testing.

Gas gun estimations based on Carlucci's Ballistics Theory [40] are used to estimate the projectile travel time in the launch tube up to the end of BT1. Under the conditions of using nitrogen at ∼8300 psi, a 150 g polycarbonate projectile will take approximately 20 ms to reach the end of BT1 (assuming no friction or leakage through the evacuated dump tank and a gun breech of diameter equal to that of the projectile). Alternatively, the same 20 ms time frame can be achieved with ∼4290 psi of helium for preliminary testing series.

Based on experimental data from UW, previous projectiles with a total launch mass (projectile + obturator) of 150 g have been launched with 1200 psi of helium in the breech and 600 psi in the inner diaphragm using a 0.032" aluminum diaphragm scored at 1000 psi on either side of the inner volume. The estimated projectile travel time in this scenario based on the Carlucci theory is 36 ms. The gas gun breech and interdiaphragm pressures are variables overall that can be tuned to adjust delay times.

To burst the double-diaphragm configuration on the start gun, the inner diaphragm volume will be vented to atmosphere. An estimate of this blowdown time can be made with the engineering assumption of constant initial reservoir conditions and choked flow through the orifice. Additionally, as the estimate uses a shorter timestamp than than the actual time for the vessel to completely drain, the estimate is conservative as the diaphragm will likely burst before the volume is completely vented. The ball valve itself will also have an actuation time around 200 ms, and the pressure may vent and burst the inner diaphragm before the valve is completely open. Assuming helium at a pressure of 600 psi blowing down through a 1/8" ball valve orifice completely open, the blowdown time of the interdiaphragm (44.45 mm diameter cylinder, 38.1 mm long) is estimated to take approximately 13 ms. With the ball valve only halfway open, the estimated time is 53 ms. An estimate for the combined ball valve opening and inner volume venting is thus on the order of ∼150 - 200 ms. Additional time to vent may occur depending on the line length on the other side of the ball valve. Details on the estimation process are in Appendix B.

After the inner volume discharges, the time it takes for the aluminum diaphragms to open are estimated. The opening time can be estimated based on the inertia of a single diaphragm petal rotating about its base as a frictionless hinge as described in Appendix C. Assuming a fully open rotation to 90 degrees at the helium breech pressure of 1200 psi, the diaphragm would take approximately 105 μs to open. Such an estimation is on a similar order of magnitude as other numerical estimates of diaphragm burst times [41, 42]. Further refining in the diaphragm bursting estimation is avoided, as the timescale is considered within the uncertainty of other estimations in the time budget.

Estimation of the time budget for the projectile to reach the end of BT1 is presented in Table 7.2.

Action	$\triangle t$ (ms)	Total Time (s)
Signal sent to the globe valve solenoid	0	0
Ball valve opens and interdiaphragm volume vents	150 - 200	0.150 - 0.200
Upstream diaphragm bursts	< 1	0.151 - 0.201
Launch tube travel time to exit of BT1	36	0.187 - 0.237

Table 7.2: Estimated time budget for the projectile to reach the end of BT1.

Based on the overlap in the presented time budgets and proposed configuration, zero delay time should be implemented for the double-diaphragm configuration upon projectile launch. The zero delay time is a starting configuration based on current experimental data and the engineering assumptions made in the time budget analysis. The delay time will be further calibrated after initial testing of this experiment is completed. Additionally, several parameters can be changed such as the location of the shock tube diaphragm, gas gun breech pressure and gas type, valve venting configurations, etc to tailor the operations as desired.

Jitter of the system has yet to be determined. Under the defined operating conditions, jitter will likely need to be less than the time it takes for the wave to travel through one tube. As the low velocity start operation is eventually intended to be applied to an alternative space launch system hundreds of meters long, the millisecond timescale jitter range will be relaxed and overall less influential on the success of the system.

7.5 Wave Interactions

The wave interactions between the projectile and expanding shock tube flow will be complex with several unknowns. One anticipated interesting gas dynamic interaction will occur when the projectile reaches the contact surface, where the shock on the aftbody of the projectile will reflect from a low impedance to high impedance environment. Acoustic impedance determines how a shock reflects through a boundary between two environments, and the specific impedance and can be determined by eq. 7.2 [43]:

$$Z = \rho * a \tag{7.2}$$

The coefficient of reflection represents the fraction of wave reflection due to acoustic impedance mismatch as determined by eq. 7.3, with the coefficient of transmission in eq. C.4:

$$R_z = \frac{Z_{driven} - Z_{driver}}{Z_{driven} + Z_{driver}} \tag{7.3}$$

$$T_z = \frac{2Z_{driven}}{Z_{driven} + Z_{driver}} \tag{7.4}$$

To estimate the impedance mismatch at the contact surface, the contact surface location needs to be determined. Several parameters are normalized and the trends of each are compared to estimate the contact surface location in Figure 7.4.

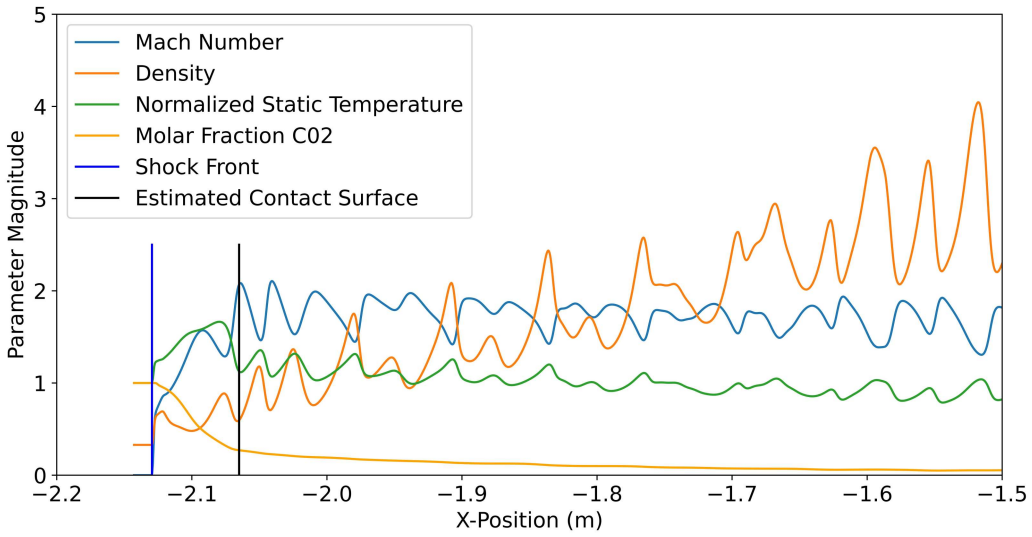

Figure 7.4: Parameter magnitudes vs. X-Position after passage through 60 baffles (4.761 ms) with estimated contact surface location.

Averaging the density and speed of sound parameters in the two regions over a length equivalent to that between the shock front and the contact surface gives a coefficient of reflection at the interface of -0.20 and a coefficient of transmission of 0.8, overall indicating the shock wave will reflect through the contact surface as a wave of the same nature. The

transmitted wave will be 80% the magnitude of the initial wave and will be traveling at a velocity slower than the projectile. This wave fall off may have negative implications for the projectile, as the projectile will immediately lose thrust as the wave and thus combustion falls behind. However, the wave may eventually be able to catch back up to the projectile, given that the combustion from the driven section is able to ignite the cold expanding driver propellant.

Chapter 8

CONCLUSION

8.1 Conclusion

Results of CFD simulations of baffled shock tubes with N2/CO2 gases at a pressure ratio of 215 indicate that the driven shock wave velocity is attenuated by approximately 75% within 13 chamber diameters from that of a corresponding smooth bore shock tube. The expansion of the driver gas through baffle chamber volumes resulted in steady degradation of total pressure that kept the contact surface in close proximity to the driven shock wave. The velocity of the contact surface was oscillatory at velocities ranging from 100 m/s to 600 m/s. These results provided a time estimate for wave arrival in the driven section that was used to determine the launch time for a projectile so that it would meet the lead shock wave near the entrance to the BTRA test section. The results of this investigation indicate that accelerating propellant toward an oncoming projectile to reduce its minimum starting speed of a BTRA is doable within the constraints of typical laboratory practices.

8.2 Prospectus

Future work involves increasing the fidelity of the CFD simulation through mesh resolution and comparing different viscosity models. Additionally, establishing a correlation between the lead shock wave attenuation with the 1-D Euler equations would be a useful analytical tool. Finally, investigation into the environment in which ignition and sustained combustion occurs during the expanding driver propellant warrants further study and experimentation. The x-t wave diagram should be worked out for the proposed scenario to give a better understanding of the state at each location within the tube, along with determining the projectile's acceleration profile.

BIBLIOGRAPHY

[1] Hertzberg, A., Bruckner, A. P., and Bogdanoff, D. W., "Ram Accelerator: A New Chemical Method for Accelerating Projectiles to Ultrahigh Velocities," *AIAAJ*, Vol. 26, No.2, 1988, pp. 195–203.

[2] Hertzberg, A., Bruckner, A. P., and Knowlen, C., "Experimental Investigation of Ram Accelerator Propulsion Modes," *Shock Waves*, Vol. 1, 1991, pp. 17–25.

[3] Knowlen, C., Joseph, B., and Bruckner, A. P., "Ram Accelerator as an Impulsive Space Launcher: Assessment of Technical Risks," *International Space Development Conference, Dallas TX*, 2007.

[4] Higgins, A. J., "Ram Accelerators: Outstanding Issues and New Directions," *Journal of Propulsion and Power*, Vol. 22, No. 6, 2006, pp. 1170–1187.

[5] Knowlen, C., Bruckner, A. P., Bogdanoff, D. W., and Hertzberg, A., "Performance Capabilities of the Ram Accelerator," *AIAA-87-2152*, 1987.

[6] Bruckner, A. P., Knowlen, C., Hertzberg, A., and Bogdanoff, D. W., "Operational Characteristics of the Thermally Choked Ram Accelerator," *Journal of Propulsion & Power*, Vol. 7, No. 5, 1991, pp. 828–836.

[7] Leege, B. J., "Advances in Baffled and Railed Tube Ram Accelerator Operation and Modeling," *Ph.D. Thesis*, University of Washington, 2022.

[8] Schultz, E., Knowlen, C., and Bruckner, A. P., "Starting Envelope of the Subdetonative Ram Accelerator," *Journal of Propulsion and Power*, Vol. 16, No. 6, 2000, pp. 1040–1052.

[9] Burnham, E. A., "Investigation of Starting and Ignition Transients in the Thermally Choked Ram Accelerator," *Ph.D. Thesis*, University of Washington, 1993.

[10] Sasoh, A., Maemura, J., Hirakata, S., Takayama, K., and Falcovitz, J., "Diaphragm Rupture. Impingement by a Conically-Nosed, Ram-Accelerator Projectile," *Shock Waves Journal*, 1999, pp. 19–30.

[11] Bruckner, A. P., Burnham, E. A., Knowlen, C., Hertzberg, A., and Bogdanoff, D. W., "Initiation of Combustion in the Thermally Choked Ram Accelerator," *18th International Symposium on Shock Waves*, 1991.

[12] Seiler, F., Patz, G., Smeets, G., and Srulijes, J., "Progress of Ram Acceleration with ISL's RAMAC 30," *Journal de Physique IV France 10*, 2000, pp. 31–41.

[13] Seiler, F., Patz, G., Smeets, G., and Srulijes, J., "Influence of Projectile Material and Gas Composition on Superdetonative Combustion in ISL's RAMAC 30," *AIAA-98-3445*, 1998.

[14] Leege, B. J., Daneshvaran, N., van Donkelaar, F., Liu, S., and Knowlen, C., "Ram Accelerator Operation in Railed and Baffled Tubes," *AIAA Propulsion and Energy forum*, 2020.

[15] Higgins, A. J., Knowlen, C., and Kiyanda, C. B., "Gasdynamic Operation of Baffled tube Ram Accelerator in Highly Energetic Mixtures," *International Colloquium on the Dynamics of Explosions and Reactive Systems*, Vol. 20th, 2005.

[16] Knowlen, C., Glusman, J., Grist, R., and Bruckner, A. P., "Experimental Investigation of a Baffled-Tube Ram Accelerator," *Propulsion and Energy Forum*, 2016.

[17] van Donkelaar, F., "Development of an Expedient Two-Stage Gas Gun," *Master's Thesis*, University of Washington, 2021.

[18] McFall, K. A., Knowlen, C., Bruckner, A. P., and Hertzberg, A., "Numerical Analysis of Zero Velocity Start Technique for the Ram Accelerator," *AIAA*, 1996.

[19] Hertzberg, A., "Method and Apparatus For Zero Velocity Start Ram Acceleration," March 1992, US Patent 5,097,743.

[20] Glass, I. I. and Hall, J. G., "Handbook of Supersonic Aerodynamics: Shock Tubes," *NAVORD Report 1488*, Vol. 6, 1959.

[21] Glass, I. I. and Sislan, J. P., "Nonstationary Flows and Shock Waves," *Oxford Engineering Science Series*, Vol. 39, 1994.

[22] Riansford, G. and Ciccarelli, G., "Visualization of Detonation Propagation in a Round Tube Equipped with Orifice Plates," *International Colloquium on the Dynamics of Explosions and Reactive Systems*, Vol. 26th, 2017.

[23] Li, J. and Ning, J., "Propogation Mechanism of Detonations in Rogh Walled Tube," *International Colloquium on the Dynamics of Explosions and Reactive Systems*, Vol. 26th, 2017.

[24] Liu, J., Lee, J. H. S., and Tan, H., "Detonation Propagation in Rough Tube," *International Colloquium on the Dynamics of Explosions and Reactive Systems*, Vol. 26th, 2017.

[25] Ago, A., Niibo, T., Tsuboi, N., and Hayashi, A. K., "Numerical Study on Effects of Obstacle Shape on Detonation Transition Mechanism," *International Colloquium on the Dynamics of Explosions and Reactive Systems*, Vol. 26th, 2017.

[26] E., C. J. and Haines, K. A., "Shock Propagation In A tube With Transverse Ribs," *12th International Symposium on Shock Tubes and Waves*, 1980.

[27] Hove, D. T. and Craig, J. E., "Airblast Attenuation Experiments for the M-X Trench," *Science Applications, Inc.*, 1978.

[28] Fry, M. A., Durrett, R. E., Ganong, G. P., Matuska, D. A., Stucker, M. D., Chambers, B. S., Needham, C. E., and Westmoreland, C. D., "The Hull Hydrodynamics Computer Code," *Air Force Weapons Laboratory*, 1976.

[29] Knowlen, C., Leege, B. J., Correy, J., Smith, C., and Higgins, A., "Baffled-Tube Ram Accelerator Operation with Methane-Air Propellant," *International Colloquium on the Dynamics of Explosions and Reactive Systems*, 2022.

[30] Leege, B. J., Smith, C., and Knowlen, C., "Baffled Tube Ram Accelerator Operation with Normal Baffles," *AIAA SciTech*, 2022.

[31] Correy, J., Leege, B. J., Bernhard, D., Ginos, J., Yancey, C., and Knowlen, C., "Investigation of Baffled-Tube Ram Accelerator Configurations," *AIAA SciTech Forum*, 2023.

[32] Yancey, C., "Performance Modeling of the Baffled Tube Ram Accelerator," *Master's Thesis*, University of Washington, 2022.

[33] Bogdanoff, D. W., Knowlen, C., Murakami, D., and Stonich, I., "Nonstationary Flows and Shock Waves," *AIAA Journal*, Vol. 28, No. 11, 1989, pp. 1942–1944.

[34] Gaetani, P., Guardone, A., and Persico, G., "Shock Tube Flows Past Partially Opened Diaphragms," *Journal of Fluid Mechanics*, Vol. 602, 2008, pp. 267–286.

[35] Sod, G. A., "A Survey of Several Finite Difference Methods for Systems of Nonlinear Hyperbolic Conservation Laws," *Journal of Computational Physics*, 1978, pp. 1–31.

[36] "ANSYS Fluent, Software Package," *Version 14.0 & 15.0*, 2019.

[37] Daneshvaran, N., "Transient Computational Fluid Dynamic Modeling of Baffled Tube Ram Accelerator," *Master's Thesis*, University of Washington, 2017.

[38] Glusman, J. F., "Theoretical Performance Model and Initial Experimentation of a Baffled-Tube Ram Accelerator," *Master's Thesis*, University of Washington, 2016.

[39] Correy, J., Bernhard, D., Ginos, J., Jalam, J. A. R., and Knowlen, C., "Mach Number Effects on Baffled-Tube Ram Accelerators," *AIAA*, 2024.

[40] Carlucci, D. E. and Jacobson, S. S., "Ballistics Theory and Design of Guns and Ammunition," 2007.

[41] Kang, M. S., Nagdewe, S., and Kim, H. D., "A Numerical Simulation on the Process of Diaphragm Opening in Shock Tube Flows," *KSPE Spring Conference*, 2008.

[42] Lyle, J. L., Guna, K. R., Kumar, P., Surdararaj, A. J., and Scholar, P. G., "Rupture Dynamics of Shock-tube Diaphragm," *First International Conference on Recent Advances in Aerospace Engineering*, 2017.

[43] Schwartz, M., "Reflection, Transmission and Impedance Lecture," Harvard University.

[44] Takiya, T., Higashino, F., Yaga, M., and Han, M., "Shock Wave Attenuation by Means of Built-in Baffles in a Tube," *Advanced Studies in Theoretical Physics*, Vol. 6, No. 5, 2012, pp. 233–244.

[45] Knowlen, C., "Theoretical and Experimental Investigation of the Thermodynamics of the Thermally Choked Ram Accelerator," *Ph.D. Thesis*, University of Washington, 1991.

[46] Knowlen, C., Byrd, T., Dumas, J., Daneshvaran, N., Glusman, J., and Bruckner, A. P., "Baffled-Tube Ram Accelerator Operation with Inclined Baffles," *AIAA Propulsion and Energy Forum*.

[47] Daneshvaran, N., Leege, B. J., and Knowlen, C., "Computational Fluid Dynamic Modeling of Railed Tube Ram Accelerator in Reactive Flow," *AIAA SciTech*, 2022.

Appendix A

EXPERIMENTAL DIAPHRAGM OPENINGS

Mylar diaphragm configurations and their respective burst pressures are shown in Table A.1. Each diaphragm had a 63.5 mm diameter, scored in an 'x' configuration (unless otherwise noted) with a 60 mm scribe, and was placed with the thinnest diaphragm facing upstream (driver section). The scored side was also faced upstream.

Diaphragm Configuration (mil)	Scoring Pressure (psig)	Burst Pressure (psi)
15 + 15	700 separately	991
15 + 15	700 separately	945
15 + 15	750 separately	928
15 + 15	850 separately	914
15 + 15	850 separately, 6 segments	670
15 + 10	850 together	793
15 + 5	850 together	635
15 + 5	850 together	579

Table A.1: Experimental diaphragm openings and their respective burst pressure.

Appendix B

INTERDIAPHRAGM BLOWDOWN ESTIMATION

A simple blowdown estimation of the start gun's interdiaphragm volume is done based on the engineering assumption of constant initial reservoir conditions and choked flow at the orifice. A characteristic time from the estimation is found to approximate the time at which the vessel is empty. The density and speed of sound ratios with sonic conditions can be determined by:

$$\frac{\rho^*}{\rho_0} = \left(1 + \frac{\gamma - 1}{2} M^2\right)^{-1/(\gamma-1)} \tag{B.1}$$

$$\frac{a^*}{a_0} = \left(1 + \frac{1}{2}(\gamma - 1) M^2\right)^{-1/2} \tag{B.2}$$

Where the subscript 0 indicates initial reservoir conditions, the superscript * indicates throat conditions, and the Mach number M is one. The mass flow rate from choked flow at the orifice can be determined by:

$$\dot{m}^* = \rho^* a^* A = \left(\frac{\rho^*}{\rho_0}\right)\left(\frac{a^*}{a_0}\right) \rho_0 a_0 A \tag{B.3}$$

Where A is the area of the orifice. The final characteristic time can then be found by:

$$t = \frac{m}{\dot{m}^*} \tag{B.4}$$

Where m is the total mass in the reservoir.

Appendix C

DIAPHRAGM PETAL OPENING ESTIMATION

The time for a diaphragm to open can be estimated based on the inertia of an individual petal. Assuming the petal is an equilateral triangle rotating about a frictionless hinge at its base, the inertia can be calculated as:

$$I_{base} = \frac{mh^2}{6} \tag{C.1}$$

Where h is the height of the equilateral triangle and m is the mass of the petal. Newton's second law for rotation is:

$$\sum \tau_f = I_{base}\alpha \tag{C.2}$$

Where τ_f is the torque acting on the petal, and α is the angular acceleration. As the petal opens, the surface area and thus torque decreases. However, a torque estimate will be provided based a constant petal area at constant pressure.

The angular acceleration can then be estimated as:

$$\alpha = \frac{\sum \tau_f}{I_{base}} = \frac{2PA}{mh} \tag{C.3}$$

Where P is the breech pressure and A is the area of the petal.

Finally, assuming the petal is initially at rest, the time for the petal to accelerate to a specified opening angle θ is:

$$t = \left(\frac{2\theta}{\alpha}\right)^{1/2} = \left(\frac{\theta mh}{PA}\right)^{1/2} \tag{C.4}$$